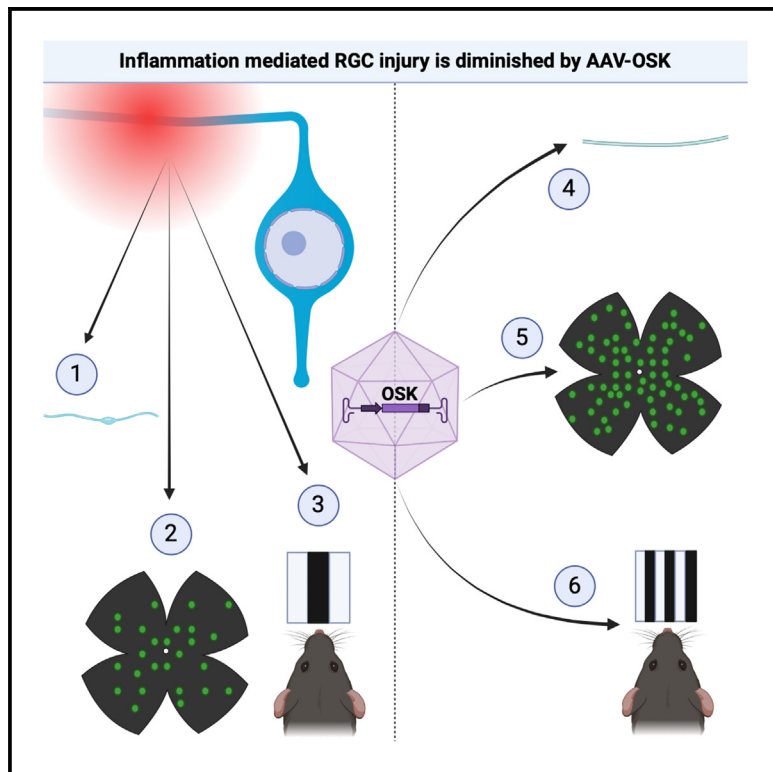


Cellular rejuvenation protects neurons from inflammation-mediated cell death

Graphical abstract



Authors

Sienna S. Drake,
Abdulshakour Mohammadnia,
Aliyah Zaman, ..., Jo Anne Stratton,
David A. Sinclair, Alyson E. Fournier

Correspondence

alyson.fournier@mcgill.ca

In brief

In this manuscript, Drake et al. describe an aging-like transcriptional signature in retinal ganglion cells during experimental autoimmune encephalomyelitis (EAE) like that of cortical neurons in patients with multiple sclerosis. Partial reprogramming with AAV2-Oct4-Sox2-Klf4 to rejuvenate the transcriptome results in improved RGC survival and visual acuity during EAE.

Highlights

- RGCs demonstrate similar gene expression changes during EAE and aging
- RGCs exhibit DNA damage, chromatin mark changes, and nuclear lamina dystrophy in EAE
- Patients with MS exhibit DNA damage and senescence-associated changes in neurons
- AAV2-OSK limits RGC death and preserves visual acuity during EAE



Article

Cellular rejuvenation protects neurons from inflammation-mediated cell death

Sienna S. Drake,¹ Abdulshakour Mohammadnia,¹ Aliyah Zaman,¹ Christine Gianfelice,¹ Kali Heale,¹ Adam M.R. Groh,¹ Elizabeth M.-L. Hua,¹ Matthew A. Hintermayer,¹ Yuancheng Ryan Lu,² David Gosselin,³ Stephanie Zandee,^{1,4} Alexandre Prat,⁴ Jo Anne Stratton,¹ David A. Sinclair,² and Alyson E. Fournier^{1,5,*}

¹Department of Neurology and Neurosurgery, Montreal Neurological Institute, McGill University, Montreal, QC H3A2B4, Canada

²Department of Genetics, Broad Institute, Harvard Medical School, Boston, MA 02115, USA

³Department of Molecular Medicine, Faculty of Medicine, Université Laval, Quebec City, QC G1V4G2, Canada

⁴Centre de Recherche du Centre Hospitalier de l'Université de Montréal (CRCHUM), Montreal, QC H2X0A9, Canada

⁵Lead contact

*Correspondence: alyson.fournier@mcgill.ca

<https://doi.org/10.1016/j.celrep.2025.115298>

SUMMARY

In multiple sclerosis (MS), inflammation of the central nervous system results in demyelination, neuroaxonal injury, and cell death. However, the molecular signals responsible for injury and cell death in neurons are not fully characterized. Here, we profile the transcriptome of retinal ganglion cells (RGCs) in experimental autoimmune encephalomyelitis (EAE) mice. Pathway analysis identifies a transcriptional signature reminiscent of aged RGCs with some senescent features, with a comparable signature present in neurons from patients with MS. This is supported by immunostaining demonstrating alterations to the nuclear envelope, modifications in chromatin marks, and accumulation of DNA damage. Transduction of RGCs with an Oct4-Sox2-Klf4 adeno-associated virus (AAV) to rejuvenate the transcriptome enhances RGC survival in EAE and improves visual acuity. Collectively, these data reveal an aging-like phenotype in neurons under pathological neuroinflammation and support the possibility that rejuvenation therapies or senotherapeutic agents could offer a direct avenue for neuroprotection in neuroimmune disorders.

INTRODUCTION

Multiple sclerosis (MS) is an immune-mediated disease with a neurodegenerative component affecting approximately 2.3 million people worldwide.¹ While immune-mediated demyelination of axons constitutes a primary pathogenic mechanism in MS, sustained clinical deficits are associated with neuronal degeneration, including loss of neurons in the gray matter and loss of axons in white matter lesions and normal-appearing white matter.^{2–4} Analyses of both non-lesioned and lesioned postmortem brain, spinal cord, and optic nerve have provided evidence of extensive and diffuse axonal degeneration and neuronal cell body loss throughout the CNS of patients with MS.^{5–12} Notably, the retina and optic nerve acquire extensive pathology in MS. Optic nerve lesions are frequently detected in patients with MS by MRI.^{13,14} Additionally, there is significant retinal nerve fiber layer and ganglion cell layer thinning evidenced by optical coherence tomography, and this correlates with clinical deficits and brain volume loss.^{10,14–22} Finally, postmortem tissue analysis of the optic nerve finds gliosis, demyelination, and axonal injury similar to MS pathology observed in other CNS regions.²³ This is mirrored in the experimental autoimmune encephalomyelitis (EAE) mouse model, where there is optic nerve demyelination, immune cell infiltration and gliosis, retinal nerve layer thinning, neuron loss, and axonal pathology, making the EAE mouse retina and optic nerve a useful

model to study inflammation-mediated neurodegeneration.^{22,24–29} Multiple agents contribute to neurodegeneration in MS and EAE. Loss of myelin sheath trophic support; noxious factors released by activated glia, infiltrating immune cells, and degenerating myelin; mitochondrial dysfunction and oxidative stress induced by reactive oxygen and reactive nitrogen species; and glutamate excitotoxicity are all evidenced to contribute to axonal and neuronal cell body injury.^{30–34} Thus, identifying neuron-intrinsic mechanisms that foster survival and resilience rather than focusing solely on neutralizing individual toxic agents may expedite the development of novel neuroprotective therapies to treat MS.

Recent studies have explored the relationships between aging, cellular senescence, and MS. In patients with MS, DNA methylation clock studies have demonstrated accelerated aging in immune cells and glial cells, and shorter telomere length, another marker of aging, is observed in peripheral leukocytes and associated with lower brain volume in patients with MS.^{35–39} Animal models have provided further evidence for the involvement of aging and cellular senescence in pathological CNS inflammation. Aged EAE animals experience a worsened disease course and extensive CNS microglial reactivity with distinct proinflammatory transcriptomic profiles compared to young EAE animals.⁴⁰ Cellular senescence is also highly correlated with aging and age-related disease.^{41–43} Although cellular senescence was



originally defined by aberrant cell cycle exit, it is also characterized by other features, including altered autophagy, the senescence-associated secretory phenotype (SASP), accumulation of DNA damage, and epigenetic changes.⁴² Targeting aging and senescence programs in MS may be a beneficial strategy to address immune cell or glial dysfunction; however, there is limited data about the neuronal gene signature in MS and thus whether rejuvenating therapies may promote neuroprotection.⁴⁴

It is certain that the complex inflamed and injurious environment alters intrinsic neuronal gene programs, as it does to CNS glial cells.⁴⁵ Indeed, RNA sequencing studies so far have demonstrated changes to neuronal gene expression in patients with MS; alterations to microRNA (miRNA) expression in EAE and patients with MS; and pathological protein accumulation in EAE.^{46–48} Notably, neurons likewise undergo significant transcriptomic changes throughout the human and mouse lifespans, and restoring a younger transcriptomic profile by overexpressing *Oct4*, *Sox2*, and *Klf4* (OSK) transcription factors promotes neuronal survival and regeneration in mice following optic nerve crush and glaucoma.^{49–52} In this study, through multimodal sequencing of retinal ganglion cells (RGCs), a similar transcriptional signature was found between young EAE RGCs and old naïve RGCs. Gene Ontology (GO) term pathway analysis identified dysregulated pathways relevant to cellular senescence in young EAE RGCs. Analysis of existing sequencing datasets for neurons from patients with MS reveals a similar enrichment for aging and cellular senescence pathways, and immunohistochemistry (IHC) of EAE retinal tissue reveals the dysregulation of several protein components of senescence. Finally, AAV-OSK-mediated rejuvenation of RGCs preserves visual acuity and protects from cell death in the EAE mouse model.

RESULTS

The RGC transcriptome in EAE resembles naïve aged RGCs

To profile the response of neurons to pathological inflammation, RGCs were enriched by fluorescence-activated cell sorting (FACS) from EAE (2–3 months old), naïve age-matched (2–3 months old), and naïve aged (6–7 months old) Thy1-vGlut2-YFP transgenic mice (Figure S1). RNA from RGC-enriched samples were sequenced, and DESeq2 was used to obtain normalized read counts and compare gene fold changes (FCs) between EAE samples and naïve age-matched samples or naïve aged samples. Linear regression analysis of the log2FC values identified a significant correlation between the FC of all detected genes in RGCs between EAE and naïve aged mice, suggesting that EAE neurons exhibit an aging signature ($R^2 = 0.47$, $p < 0.001$; Figure 1A). By assessing all significantly dysregulated genes, we found that over 50% of the upregulated genes in EAE mice were also significantly upregulated in naïve 6-month-old mice and over 50% of genes significantly downregulated in EAE RGCs were also downregulated in 6-month-old RGCs, further supporting a common signature of gene expression patterns between young EAE and old naïve RGCs (Figure 1B). To validate this finding, an external RNA sequencing dataset of 12-month-old RGCs and 5-month-old RGCs was obtained from the NIH BioProject (NCBI: PRJNA655981) and reanalyzed

following the same workflow to obtain gene expression changes between the 12-month-old and 5-month-old RGCs, and a list of the top 100 significantly upregulated genes in the 12-month-old RGCs was generated.⁴⁹ Here, ranked gene set analysis showed significant enrichment of this gene list in both the 6-month aged RGCs and EAE RGCs, further suggesting that genes upregulated during aging in RGCs are likewise being upregulated in young inflamed RGCs (Figures 1C and 1D). Senescence, one hallmark of cellular aging, is a collection of altered cellular pathways and dysregulated gene expression that often arises in aged cells and has been predominantly characterized in non-neuronal cells where ongoing cell division, causing replicative stress, induces departure from the cell cycle.⁴² Although neurons have undergone terminal differentiation, aged neurons exhibit characteristics of senescence, including DNA damage and elevated expression of proinflammatory molecules.^{53,54} To compare our neuronal signature to classically defined senescence genes, ranked gene set enrichment was conducted comparing the EAE RGCs, 6-month RGCs, and aged RGC data to a curated senescence gene set. This gene set (SEN_MAYO) contains genes known to be involved in senescence and commonly upregulated in aging, with classifications as cytokines/chemokines, transmembrane proteins, or intracellular proteins, and is consistently enriched in various aged tissue samples across mice and humans.⁵⁵ Here, ranked gene set enrichment found significant enrichment of the SEN_MAYO gene set in all three gene expression datasets: EAE, 6-month-old RGCs, and 12-month-old RGCs (Figures 1E–1G). Indeed, the 12-month-old RGCs had the largest normalized enrichment score (NES = 2.12), followed by EAE RGCs (NES = 1.72) and finally by 6-month-old RGCs (NES = 1.38), suggesting that inflamed RGCs exhibit features of senescence (Figures 1E–1G). One common feature of senescence is the SASP, which consists of the upregulation of a group of secreted inflammatory factors. Thus, the SEN_MAYO gene set was subsetted based on the genes' prior classification as cytokines/chemokines (CYTO) to evaluate the contribution of inflammatory secreted molecules to the senescence phenotype compared to the contribution of the non-cytokine/chemokine genes (transmembrane and intracellular classification, NOT_CYTO; see Table S1). While there was a significant contribution of cytokines/chemokines to the EAE signature (Figure 1E), both SEN_MAYO gene subsets were significantly enriched, suggesting that both inflammatory genes and other genes contribute to the senescence-like phenotype in EAE neurons (Figure 1E). In 12-month-old RGCs, the CYTO gene subset made a comparatively smaller contribution ($p = 0.05$), which affirms the stronger inflammatory component of EAE compared to natural aging (Figure 1F). In the 6-month-old RGCs, neither subset on its own reached statistical significance, evidencing the lower level of senescence at this age (Figure 1G). Finally, an RNA sequencing dataset from motor neurons of EAE mice was evaluated for the SEN_MAYO gene sets.⁴⁸ Similarly, the SEN_MAYO gene set was significantly enriched in EAE motor neurons, with significant enrichment from both the CYTO and NOT_CYTO subsets (Figure 1H). Overall, these data demonstrate that inflamed RGCs appear transcriptionally older and acquire a gene signature with features of senescence that is likewise present in EAE motor neurons and consists of transcripts

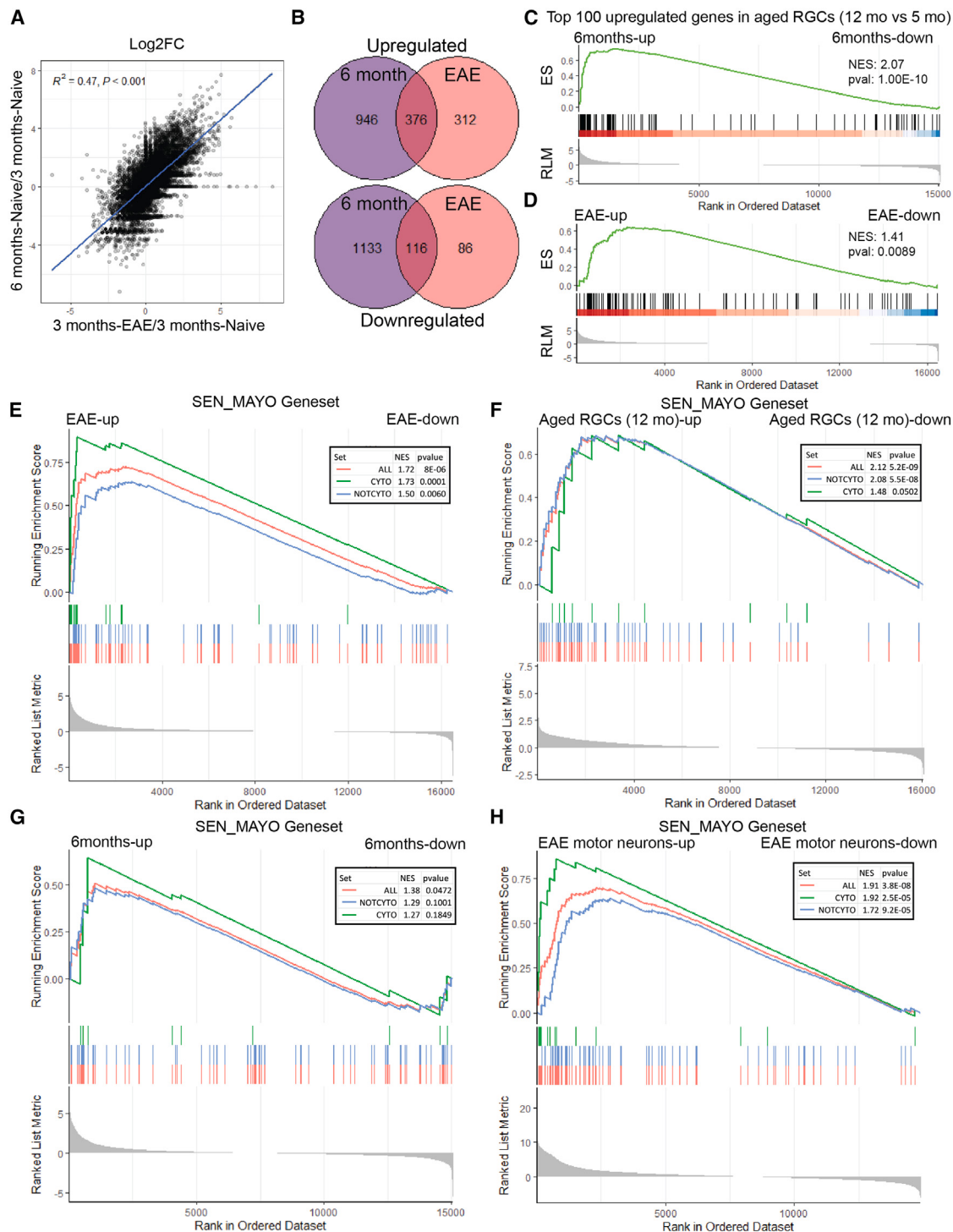


Figure 1. Age-associated changes in the transcriptome of RGCs from EAE mice

(A) log2FC for each gene of 6-month-old naive RGCs (y axis) versus 3-month-old EAE RGCs (x axis), with a linear regression curve fit to the data.

(B) Overlap between significantly (p adj. < 0.05) upregulated (top) and downregulated (bottom) genes in 6-month-old naive and 3-month-old EAE RGCs, with the number in the bubbles referring to the count of genes in each set.

(C and D) Ranked gene set enrichment result of the top 100 upregulated genes in aged RGCs for 6-month-old (C) and EAE (D) RGCs.

(E–H) Ranked gene set enrichment result for the SEN_MAYO gene set, split by the classification cytokine/chemokine, for EAE RGC (E), aged RGC (F), 6-month-old RGC (G), and EAE motor neuron (H) samples.

ES, enrichment score; RLM, ranked list metric; NES, normalized enrichment score.

from both non-secreted proteins and secreted inflammatory proteins.

Gene co-expression across the EAE disease course identifies altered pathways relevant to senescence

To more fully describe how gene expression was changing in RGCs during EAE, gene co-expression analysis was conducted comparing 3-month-old naïve, 3-month-old presymptomatic, and 3-month-old symptomatic EAE RGC samples (Figure 2A). Eight gene modules with at least 300 gene members each were identified, grouping genes with different patterns of expression across the disease course (Figure 2B). Using assay for transposase-accessible chromatin (ATAC) sequencing data generated from FACS-enriched RGCs, the accessibility of the transcription start site (TSS) of all module genes was subdivided into quartiles ranging from least accessible (quartile 1) to most accessible (quartile 4). The genes present in the eight modules were enriched for highly accessible genes (predominantly quartiles 4 and 3), indicating that these are true RGC-expressed genes based on their expression and accessibility (Figure 2C). Next, GO biological process (BP) term enrichment was conducted for each module. A large portion of enriched GO terms were specific to each module, with some overlap, as a result of the unique gene sets of each module (Figure 2D). Based on the hallmarks of aging, GO terms related to these processes were assessed in each module, with a focus on those related to DNA damage, autophagy and proteostasis, mitochondrial energy maintenance, the cell cycle, senescence, and histone modifications⁴¹ (Figure 2E). DNA damage- and cell-cycle-associated pathways were particularly enriched in module 4, which consists of genes that increase expression at the symptomatic phase of EAE. Pathways related to histone modifications were enriched in module 2, which consists of genes that decrease throughout presymptomatic and symptomatic EAE. Module 3, consisting of genes that are increased at both presymptomatic and symptomatic EAE, demonstrated significant enrichment of terms related to cellular senescence and had a preponderance of pathways relevant to inflammation and chemotaxis. Module 1, consisting of genes that increase at symptomatic EAE, demonstrated enrichment of mitochondrial- and energy-associated pathways, as well as pathways related to the unfolded protein response, cell stress, and apoptosis. Modules 5 and 7, which decrease in symptomatic EAE, demonstrated enrichment of pathways related to neuronal processes such as synaptic transmission and dendrite morphology (Figures 2E and 2F). Lastly, modules 6 and 8 consisted of genes that were upregulated and downregulated at presymptomatic EAE, respectively, with module 6 consisting of terms related to protein folding and localization and module 8 with terms related to mRNA splicing (Figure 2F). In sum, gene groups that increased were enriched for terms related to inflammation, cell stress, cell cycle and senescence, and the DNA damage response, whereas gene groups that decreased were enriched for pathways related to epigenetic regulation and neurotransmission. Together, these analyses provide further evidence for alterations in senescence-associated processes in RGCs.

A senescent transcriptional signature is present in cortical neurons from patients with MS

To determine whether features of senescence detected in the EAE RNA sequencing samples were similarly dysregulated in neurons from patients with MS, an online available single-nucleus sequencing dataset was accessed and reanalyzed to assess average gene expression across all identified neuronal clusters present in both control samples and samples from patients with MS.⁴⁶ Here, 10 neuronal cell clusters were identified, 8 of which had more than 5 cells present in both MS and control samples, which were used for downstream expression averaging and analysis (Figure 3A). Average neuronal gene expression was computed for all neurons per patient, and then single-sample gene set enrichment analysis (GSEA) was conducted to calculate an enrichment score for the SEN_MAYO gene set in each patient, as well as the CYTO and NOT_CYTO subsets. As expected, pathways related to axonal and dendrite integrity were de-enriched in MS patient neurons, validating previous findings of neuronal degeneration as a feature of MS pathology^{56,57} (Figure S2). Additionally, MS neurons demonstrated significant enrichment of the SEN_MAYO gene set compared to control patient neurons. Both CYTO and NOT_CYTO subsets were significantly enriched in MS neurons, revealing a contribution of both non-secreted senescence-associated factors and secreted inflammatory senescence-associated genes (Figure 3B). Next, GO term GSEA was conducted, and BPs related to senescence, DNA damage, the cell cycle, and epigenetic modifications were evaluated. The overlap of de-enriched and enriched pathways in neurons from patients with MS were compared to the GO terms enriched in the downregulated gene modules in symptomatic EAE (modules 2, 5, and 7) and upregulated modules in symptomatic EAE (modules 1, 3, and 4), respectively (Figures 3C and 3D). Despite comparing between bulk sequencing and single-nucleus sequencing and between human and mouse gene sets, there were common pathways identified between the two, particularly for the enriched pathway group, where almost a quarter of pathways occurred in at least one of the related EAE modules (Figure 3D). Notably, pathway overlap was observed between pathways enriched in MS patient neurons and EAE module 3 (67 pathways, 12% of the total), which consisted of immune-system- and inflammation-related GO terms (Figure 3D). Overlap with EAE module 1 and module 4 contributed an additional 4% and 3% of pathways, respectively, here with M1/MS overlap consisting of terms like “response to unfolded protein” and “ER overload response” and M4/MS overlap consisting of terms including “positive regulation of DNA repair” and “positive regulation of telomere maintenance in response to DNA damage.” 16 pathway terms (3%) were shared between EAE module 1 and EAE module 3 and enriched in MS neurons including “cellular respiration” and “ATP biosynthetic process.” Additionally, numerous pathways were significantly dysregulated related to the same hallmarks of aging: DNA damage, cell cycle and senescence, mitochondrial dysfunction, and histone modifications (Figures 3E–3H). This suggests that in MS, similar to EAE, neurons demonstrate enrichment of genes related to senescence and alteration of pathways relevant to the processes of aging and senescence, including DNA damage, epigenetic modifications, and mitochondrial dysfunction.

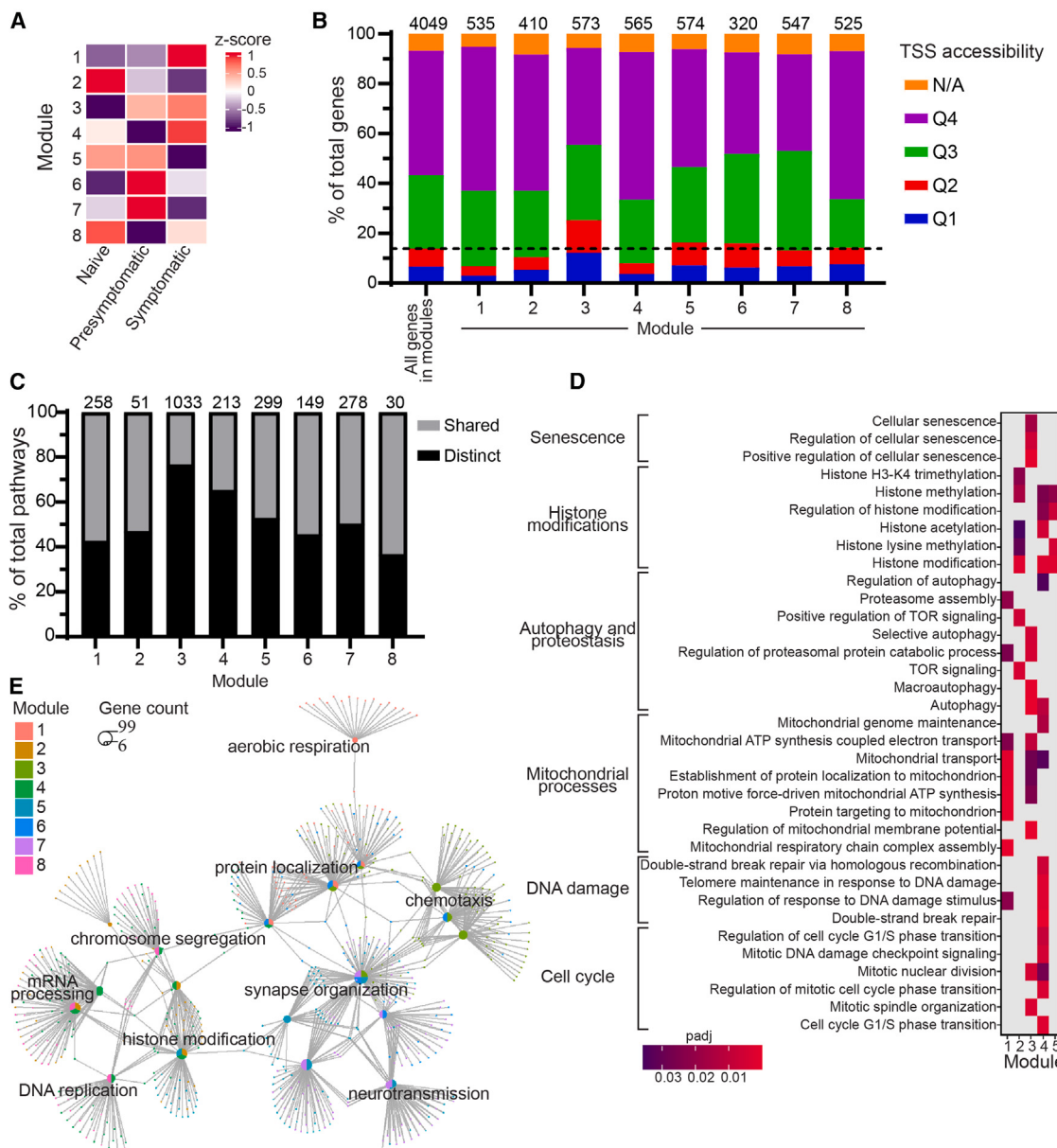


Figure 2. Gene co-expression across EAE disease course identifies altered pathways related to senescence in EAE

- (A) Diagram of EAE disease course showing a typical worsening ascending motor paralysis score over time post-disease induction (DPI) and time points and motor symptom scores collected for sequencing analysis.
- (B) Leiden-based clustering of genes that change from naive, presymptomatic (7 DPI, score: 0) to symptomatic EAE (12–16 DPI, score: >0) identified 8 gene co-expression modules.
- (C) Transcription start site (TSS) accessibility in quartiles of genes assigned to modules, count of total genes per module listed on top of the bar for each module.
- (D) Percentage of distinct significantly enriched (p adj. < 0.05) GO BPs for each module, with the count of total number of pathways per module listed at the top of each bar.
- (E) Subset of significantly enriched GO BPs displayed related to pathways involved in senescence, showing enrichment across modules 1–5.
- (F) Simplified network diagram showing top GO terms per module and their relationships to other modules.

Senescence-related protein changes are present in EAE RGCs and cortical neurons from patients with MS

With a transcriptomic signature suggesting senescence-related processes in EAE neurons, protein markers of senescence were assessed by IHC in EAE retinal cross-sections to validate

that these pathway-level changes were reflected at a protein level. One common feature of senescence is the accumulation of DNA damage, which likewise occurs in aged neurons.^{54,58} Given the evidence for alterations to DNA damage pathways at the transcriptomic level, this was assessed in EAE retinal tissue

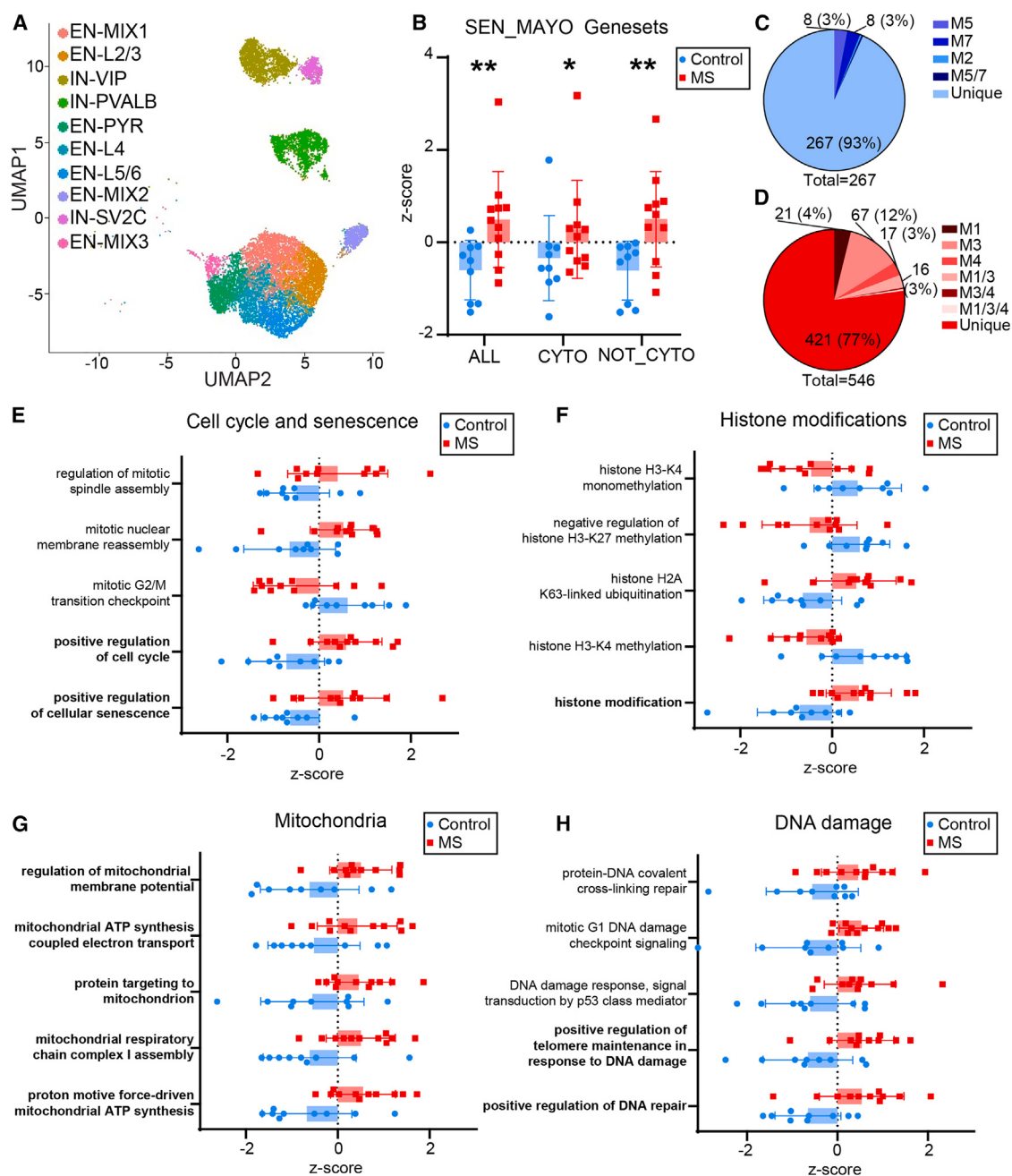


Figure 3. Single-nucleus sequencing of neurons from patients with MS identifies senescence-associated changes

(A) Uniform manifold approximation and projection (UMAP) representation of ten neuronal cell clusters identified from single-nucleus sequencing of MS and control gray matter in Schirmer et al.⁴⁶ Clusters EN-MIX2 and EN-MIX3 were only identified in patients with MS (5 or less cells in control samples) and excluded from the downstream analysis.

(B) SEN_MAYO gene set enrichment in patients with MS compared to controls. * $p < 0.05$ and ** $p < 0.01$; one-tailed Mann-Whitney test. Error bars: standard deviation.

(C) De-enriched GO BP terms in patients with MS compared to controls and their overlap with EAE module 2 (M2), M5, and M7; comparisons with an overlap of $\geq 3\%$ are annotated.

(D) Enriched GO BP terms in patients with MS compared to controls and their overlap with EAE M1, M3, and M4; comparisons with an overlap of $\geq 3\%$ are annotated.

(E-H) Subset of significantly dysregulated GO terms related to cell cycle and senescence (E), histone modifications (F), mitochondria (G), and DNA damage (H), all significant at p adj. < 0.05 . Bolded terms reflect their significant enrichment in one or more EAE modules. Error bars: standard deviation.

through γH2AX immunoreactivity (Figures 4A and 4B). Here, there was a significant increase in the number of BRN3A-positive (BRN3A+) RGC nuclei with γH2AX positivity in EAE RGCs compared to naive age-matched mice at symptom onset (10–12 days post-induction [DPI]), and it was even higher at peak motor symptoms (14–18 DPI) (Figure 4C). Using higher-resolution microscopic imaging, we obtained images that could resolve even small γH2AX foci in the RGC nuclei of naive animals and used these images to quantify the mean number of γH2AX foci per BRN3A+ nuclei. Again, there was a strong enrichment in EAE RGCs for γH2AX nuclear foci (Figures 4D–4F). Next, histone modifications were evaluated by IHC for H3K27 trimethylation (H3K27me3) (Figures 4G and 4H). While this mark may be up- or downregulated in senescent cells, there is evidence that in aged neurons, it is upregulated.⁵⁹ Similarly, increased fluorescence intensity of nuclear H3K27me3 was observed in the EAE animals, notably only reaching significance at peak disease, compared to naive control mice (Figure 4I). Another common feature of senescent cells is the loss of nuclear envelope integrity, evidenced by IHC for nuclear lamina proteins.^{60,61} Here, LAMINB1 IHC was conducted to assess the nuclear lamina morphology in RGCs in EAE (Figures 4J and 4K). Compared to naive control mice, EAE mice, even at symptom onset, had an increased number of RGCs with abnormal or dystrophic nuclear envelopes, as defined by incomplete or highly invaginated nuclear laminae (Figure 4L). Together, these data suggest that RGCs in EAE mice demonstrate dysregulation of proteins related to aging and senescence across the disease time course. Importantly, postmortem tissue containing cortical gray matter from patients with MS was likewise assessed for DNA damage by IHC for γH2AX (Figures 5A–5H). Signal intensity was notably less diffuse and more aggregated in neuronal nuclei from patients with MS compared to sections from patients with non-neurological disease (Figures 5G and 5H). Additionally, quantification of the mean and max pixel intensity of γH2AX in NeuN+ cortical neurons was higher, on average, in neurons from patients with MS compared to surgically resected cortical gray matter tissue from patients with non-neurological disease (Figures 5I and 5J).

Overexpression of rejuvenating transcription factors OSK preserves RGCs in EAE

Given the remarkable age-related and senescent signature detected by RNA sequencing and IHC in the RGCs of EAE mice, an AAV gene therapy approach previously demonstrated to rejuvenate RGCs was employed to assess whether this may also aid neurons in response to inflammatory injury. This approach was previously shown to restore a youthful DNA methylation and transcriptional signature to aged RGCs and protect from cell death in an age-related neurodegenerative disease model of glaucoma.⁴⁹ AAV2-GFP and AAV2-OSK (vector containing an Oct4-Sox2-Klf4 gene construct) were injected intravitreally 3 days prior to EAE induction (DPI). Animals were monitored daily for motor symptom scoring from 7 until 18 DPI, at which time the tissue was collected for viral transduction assessment in the retina and RGC survival quantification (Figures 6A and 6B). No significant difference was observed in EAE motor score progression or severity, as the AAV expression through intravitreal injec-

tion is restricted to the RGCs⁴⁹ (Figure 6B). Remarkably, visual acuity, assessed by optomotor response, was significantly higher in the AAV2-OSK compared to AAV2-GFP mice at peak disease (Figure 6C). Next, retinal flat mounts were evaluated by IHC for GFP to label AAV2-GFP-transduced cells or by IHC for KLF4 to label AAV2-OSK-transduced cells (Figure 6D). Then, GFP+ and KLF4+ RGCs were quantified by colocalization of the GFP or KLF4 signal with the RGC marker RBPMs. Compared to naive AAV2-GFP animals, EAE AAV2-GFP animals demonstrated a significant reduction of GFP+ RGCs, suggesting that these RGCs are dying throughout the disease course, in line with previous findings of RGC death in EAE (Figures 6D and 6E).²⁹ In contrast, EAE AAV2-OSK retinas retained the same number of transduced cells as their naive counterparts, suggesting that AAV2-OSK-transduced RGCs survive longer in EAE (Figures 6D–6F). Indeed, overall quantification of the total number of RGCs across the retinae found that EAE AAV2-OSK retinas had significantly more RGCs compared with EAE AAV2-GFP retinas (Figure 6G). Intriguingly, overall RGC count was strongly correlated with visual acuity (Figures S3B and S3C). Axonal and dendritic pathology was subsequently assessed in tissue sections. Axon swellings were quantified in presymptomatic and peak disease EAE optic nerves from AAV2-OSK- and AAV2-GFP-transduced animals (Figure 6H). These swellings did not overlap with nuclei, confirming their axonal localization (Figure S4A). There was a significant increase in swelling from presymptomatic to peak disease in the AAV2-GFP animals, mimicking what has been reported previously on axonal swellings in EAE²² (Figure 6I). However, the AAV2-OSK animals did not demonstrate a significant increase in axonal swellings (Figure 6I). Additionally, dendritic layer thickness was quantified from immunohistochemical imaging of retinal cross-sections (Figure 6J). Here, the thickness of the dendritic layer was significantly decreased in AAV2-GFP animals compared to naive and AAV2-OSK animals (Figure 6K). This was validated by hematoxylin and eosin tissue labeling and MAP2 IHC to label the inner plexiform layer (IPL) (Figures S4B–S4E). H3K27me3 fluorescence intensity was compared between AAV2-GFP- and AAV2-OSK-transduced RGCs to evaluate whether OSK would affect previously identified histone modifications occurring in EAE animals, as H3K27me3 fluorescence intensity was shown to increase in RGCs in EAE. A significant reduction in H3K27me3 fluorescence intensity was observed in the AAV2-OSK-transduced RGCs compared to AAV2-GFP RGCs (Figures 6L–6N). Finally, nuclear envelope integrity by LAMINB1 IHC was evaluated, and here again, AAV-OSK-transduced RGCs demonstrated fewer abnormal nuclear envelopes compared to AAV-GFP-transduced RGCs (Figures 6O–6Q). Together, these data demonstrate that AAV2-OSK protects RGCs during inflammation-mediated axonal and dendritic injury and cell death and improves visual function while remediating some histone and nuclear envelope changes that occur during the EAE disease course in RGCs.

Overexpression of OSK reverses changes in gene expression in EAE RGCs

To gain insight into how AAV2-OSK may promote RGC resilience in EAE, RNA sequencing of FACS-enriched RGCs from EAE mice

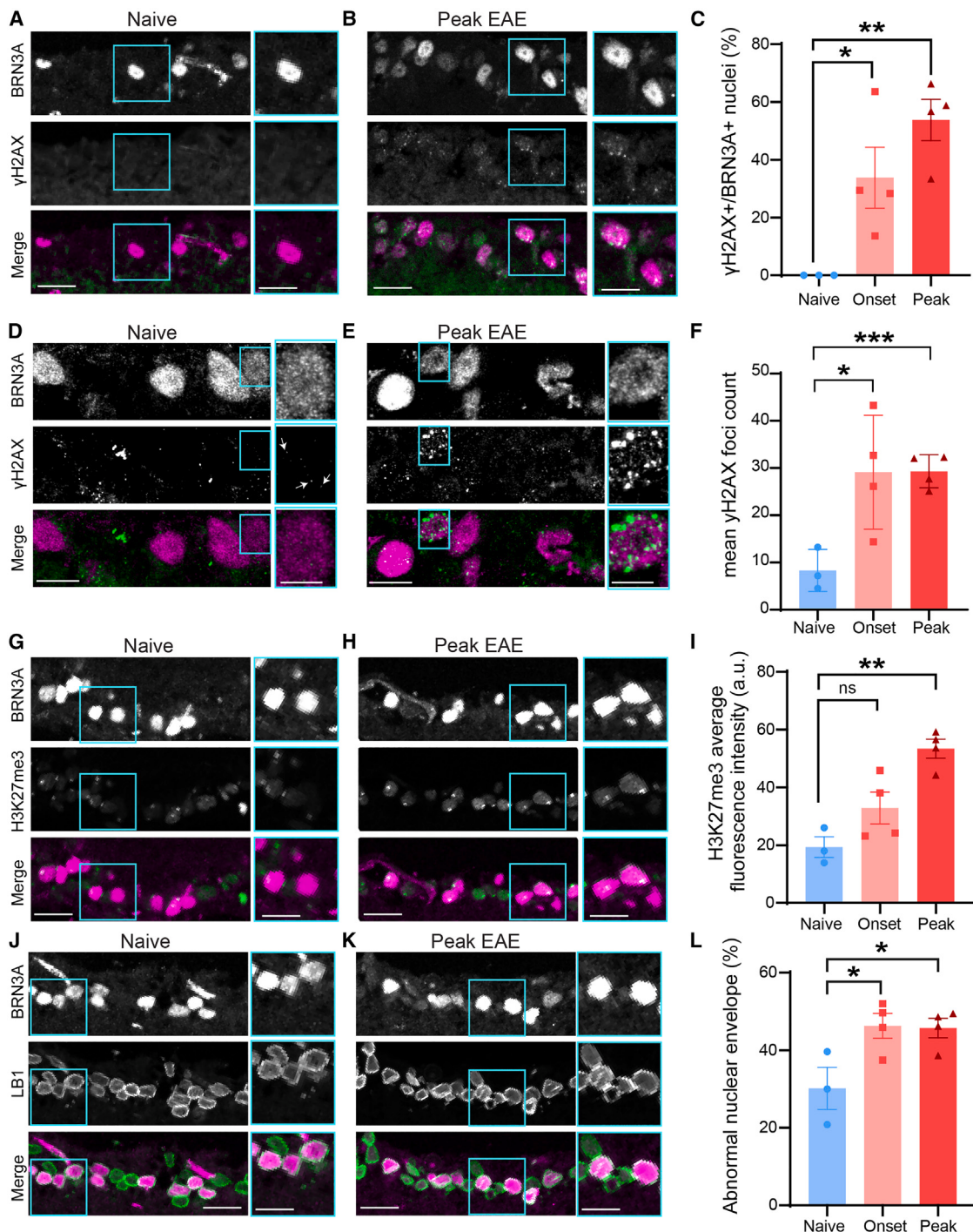


Figure 4. Immunohistochemical analysis of EAE retina detects changes in aging and senescence-associated protein markers

(A–F) Immunohistochemical analysis of γ H2AX in the RGC layer of naive (A and D) and peak EAE (B and E) mice. BRN3A in magenta labels RGCs, and γ H2AX in green (A and B) is detected in the nuclei of RGCs in EAE mice at symptom onset (10–12 DPI, score: 0.5–1.5) and peak disease (12–18 DPI, score: >1.5) (C). Higher-resolution imaging enables identification of small nuclear foci in naive animal nuclei and quantification of the number of foci per nucleus (D–F).

(G–I) Immunohistochemical analysis of H3K27me3 in the RGC layer of naive (G) and peak EAE (H) mice. BRN3A in magenta labels RGCs and H3K27me3 in green (G and H), with average nuclear fluorescence intensity quantified in (I).

(J–L) Immunohistochemical analysis of LAMINB1 (LB1) in the RGC layer of naive (J) and peak EAE (K) mice. Abnormal nuclear envelopes, as defined by incomplete or invaginated rings, are quantified in (L).

* $p < 0.05$ and ** $p < 0.01$; unpaired Student's t test. Error bars: standard deviation. Scale bars in (A), (B), (G), (H), (J), and (K) represent 25 μ m and 12.5 μ m in the zoomed inset. Scale bars in (D) and (E) represent 10 μ m and 5 μ m in the zoomed inset.

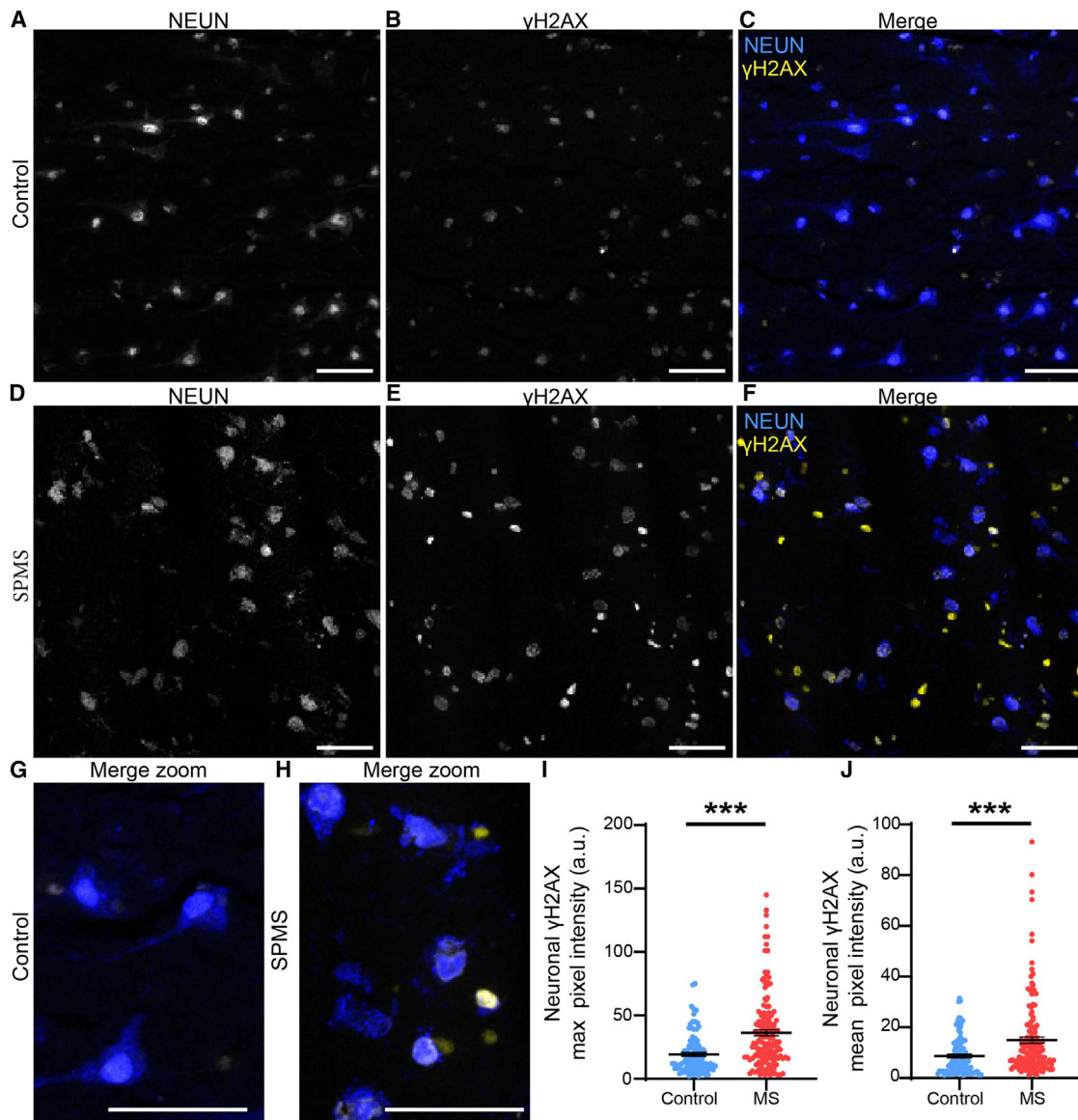


Figure 5. Immunohistochemistry detects DNA damage in cortical neurons from patients with MS

(A–C) Representative image of cortical neurons from control patient gray matter fluorescently labeled for NEUN and γ H2AX.

(D–F) Cortical neurons labeled for NEUN and γ H2AX from rapid autopsy of a patient with secondary progressive MS (SPMS).

(G and H) Higher-magnification images of merged NEUN and γ H2AX labeling of control (G) and SPMS (H) patients, demonstrating the diffuse nuclear signal of γ H2AX in control patients compared to aggregated and focal signals in SPMS patient tissue.

(I and J) Quantification of NEUN+ γ H2AX signal in control and MS tissue, demonstrating significantly higher max pixel intensity (I) and mean pixel intensity (J) in MS neurons. *** $p < 0.001$; two-tailed unpaired Student's t test. Error bars: standard deviation.

Scale bar represents 100 μ m. 50 neurons per patient were used for analysis (control $n = 2$, 100; MS $n = 3$, 150).

with AAV2-OSK or control virus was conducted (Figure 7A). Again, AAV2-OSK had no effect on the clinical motor score of animals (Figure 7B). Differential gene expression between AAV2-OSK virus and control virus (AAV2-tTA) was performed, and up-regulated genes in each group were used for pathway analysis to evaluate pathway-level changes occurring in OSK-transduced EAE RGCs. Pathways related to synaptic plasticity, learning and memory, and cognition were significantly enriched in AAV2-OSK-transduced EAE RGCs (Figure 7C). Pathways

related to cytokine production, angiogenesis, and protein localization were enriched in control AAV-tTa EAE RGCs (Figure 7C). Next, genes significantly regulated ($p < 0.05$) in both symptomatic EAE (compared to naive age-matched controls) and AAV-OSK (compared to AAV-tTa at peak EAE) were assessed. Here, a strong negative correlation was found between the genes that were dysregulated in both datasets, suggesting that for genes dysregulated in EAE, these genes are oppositely regulated with AAV2-OSK (Figure 7D). A heatmap of the genes

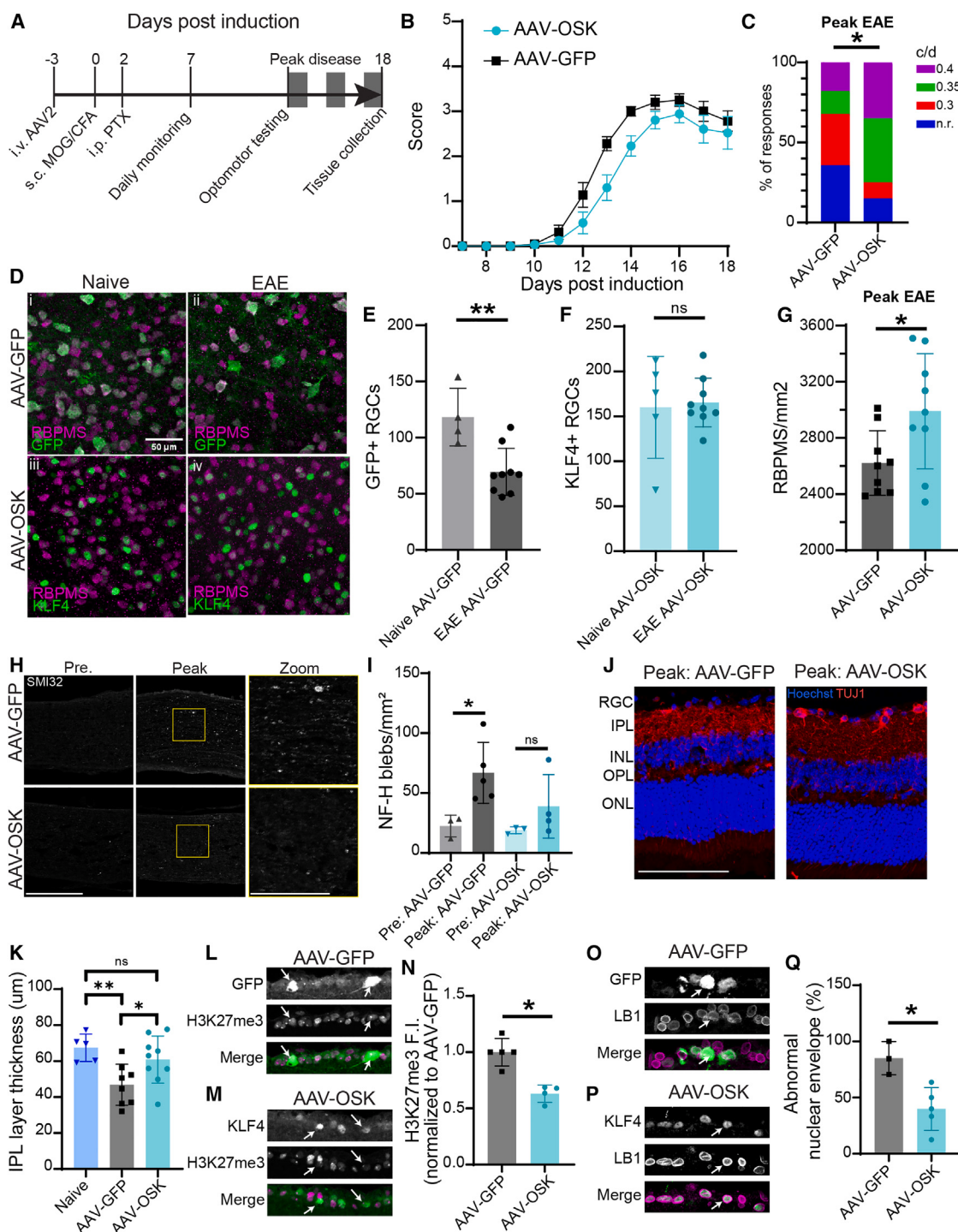


Figure 6. AAV2-OSK transduction of RGCs protects from cell death and axonal pathology and maintains visual acuity in EAE

(A) Diagram of experimental timeline showing AAV2-GFP/AAV2-OSK bilateral intravitreal (i.v.) injection 3 days pre-EAE induction (DPI), followed by EAE induction through MOG/CFA subcutaneous (s.c.) injection and pertussis toxin intraperitoneal (PTX i.p.) injection and daily monitoring of EAE score beginning at 7 DPI and continuing until the experiment end at 18 DPI.

(B) EAE disease course for animals receiving AAV2-GFP and AAV2-OSK, demonstrating no difference in motor score severity. Error bars: standard error of the mean.

(legend continued on next page)

differently regulated in symptomatic EAE and AAV-OSK EAE was generated, comparing Z scores across all sequencing data generated in this manuscript (presymptomatic EAE, symptomatic EAE, naive 3-month-old, naive 6-month-old, AAV-OSK EAE, and AAV-tTa EAE animals). Heatmap visualization confirmed not only the differential regulation of these genes between symptomatic EAE and AAV2-OSK EAE but also their similar dysregulation in 6-month-old naive animals and a trend toward to their changing expression at presymptomatic EAE (Figure 7E). *Lamb1* (Lamin B1) was notably downregulated in symptomatic EAE and naive 6-month-old animals and upregulated in AAV2-OSK EAE animals, implicating the nuclear lamina in aging and EAE at the RNA level (Figure 7E). Other genes of note included *Elapor1* and *Elapor2*, which are components of the autophagic pathway, further implicating alterations to the autophagic pathway (Figure 7E). *Bcl2a1b*, a BCL2 family member gene strongly implicated in cellular senescence, was also upregulated in symptomatic EAE and downregulated in AAV2-OSK. Pathway-level analysis of the list of genes differently regulated between symptomatic EAE and AAV2-OSK EAE indeed implicated regulation of autophagy, as well as terms related again to synaptic plasticity and learning, response to axon injury, apoptotic signaling, and oxidative stress (Figure 7F). Together, these data suggest that AAV2-OSK may revert gene expression changes occurring in RGCs during EAE that alter processes related to neuronal function, nuclear integrity, autophagy, stress, and apoptosis.

DISCUSSION

While aging and senescence are not the same, aging and age-related injury can induce senescence in cells, and depleting senescent cells can improve age-related diseases; thus, they are closely intertwined.^{42,43} The phenotype of senescent cells is varied and complex, including features such as DNA damage, nuclear lamina dysfunction, epigenetic modifications, and a SASP.⁴² However, due in part to its initial discovery as an adap-

tation of proliferative cells to stop dividing following stress or injury, it is less clear what a senescent neuron might look like given its post-mitotic nature.⁴² Here, we took a dual approach, acquiring evidence by comparing senescent neurons to aging RGCs and assessing gene sets and phenotypes related to senescence, as it is expected that a senescent neuronal phenotype would be more common in neurons from aged animals. The findings that inflamed neurons from EAE mice both appear transcriptionally alike to neurons from naive aged mice and that both EAE and aged RGCs exhibit enrichment for senescence genes and processes suggest that inflammation-mediated injury to the CNS can promote a premature aging phenotype with senescence features in neurons. The exact mediators and components of the MS and EAE inflammatory environment that drive this signature in neurons remains to be clarified, although in non-human primates, evidence exists for microglial subpopulations contributing to motor neuron senescence.⁶² Importantly, neurons exhibit cytokine and chemokine upregulation, which may promote positive feedback between the acute inflammatory injury in MS lesions and recruitment, engagement, and maintenance of inflammatory mediators throughout the CNS. Notably, this transcriptomic signature is broadly conserved across diverse neuronal cell types, including RGCs and motor neurons in EAE and both excitatory and inhibitory cortical neurons in patients with MS. Our findings also suggest that H3K27me3 is associated with inflammation and injury in EAE RGCs, a mark that has previously been reported to increase with age in cortical neurons.⁵⁹ Intriguingly, H3K9me3, a canonical senescent cell histone modification, was not notably present as assessed by IHC in either naive or EAE RGCs. However, upon induction of RGCs with AAV2-OSK, there was a strong label for H3K9me3 by IHC that was not present in AAV2-GFP-transduced RGCs in EAE (data not shown). This suggests that injury and aging may drive distinct epigenetic modifications in neurons compared to those classically studied in aging and senescence.

Indeed, the systematic evaluation of age-related changes and senescence in neurons is a relatively new endeavor; however,

(C) Visual acuity testing by optomotor response quantification demonstrates significant difference between AAV2-GFP and AAV2-OSK mice at peak EAE disease. c/d, cycles/degree; n.r., no response at tested levels. * $p < 0.05$; chi-squared test. AAV2-GFP $n = 28$, AAV2-OSK $n = 20$.

(D) Representative images of retinal flat mounts of AAV2-GFP (i/ii) and AAV2-OSK (iii/iii) naive and EAE mice showing RBPMs labeling retinal ganglion cells, GFP labeling virus-transduced GFP RGCs, and KLF4 labeling OSK-virus-transduced RGCs.

(E) Count of GFP+/RBPMs+ cells in highest-density region of retinal flat mount, demonstrating a reduction in GFP+ RGCs in EAE compared to naive mice. Error bars: standard deviation.

(F) Count of KLF4+/RBPMs+ cells in highest-density region of retinal flat mount, demonstrating no change in the number of OSK-transduced RGCs between naive and EAE mice. Error bars: standard deviation.

(G) Count of total RBPMs+ cells quantified across the retina in EAE AAV2-OSK and EAE AAV2-GFP control mice, demonstrating a greater number of RGCs remaining in retina of EAE AAV2-OSK-receiving mice compared to control. * $p < 0.05$ and ** $p < 0.01$; unpaired two-tailed Student's t test. Error bars: standard deviation.

(H) Neurofilament H (SMI-32) labeling of EAE optic nerve from AAV2-GFP- and AAV2-OSK-transduced animals at presymptomatic and peak EAE time points. Scale bar represents 250 μ m, and the zoom inset scale bar represents 100 μ m.

(I) Quantification of NF-H particle count in presymptomatic and peak EAE optic nerves from AAV2-GFP- and AAV2-OSK-transduced animals. * $p < 0.05$ unpaired two-tailed Student's t test. Error bars: standard deviation.

(J) Retinal cross-section labeled with Hoechst and Tuj1 from AAV2-GFP- and AAV2-OSK-transduced mice. Scale bar represents 100 μ m.

(K) Quantification of thickness of the IPL in naive or AAV2-GFP- and AAV2-OSK-transduced animals at peak EAE. * $p < 0.05$ and ** $p < 0.01$; unpaired two-tailed Student's t test. Error bars: standard deviation.

(L–N) Representative images and quantification of H3K27me3 fluorescence intensity in AAV2-GFP- or AAV2-OSK-transduced RGCs. Fluorescence intensity measurements presented as values normalized to AAV-GFP controls. * $p < 0.05$; unpaired two-tailed Student's t test. Error bars: standard deviation.

(O–Q) Representative images and quantification of abnormal nuclear envelopes in AAV2-GFP- or AAV2-OSK-transduced RGCs. * $p < 0.05$; unpaired two-tailed Student's t test. Error bars: standard deviation.

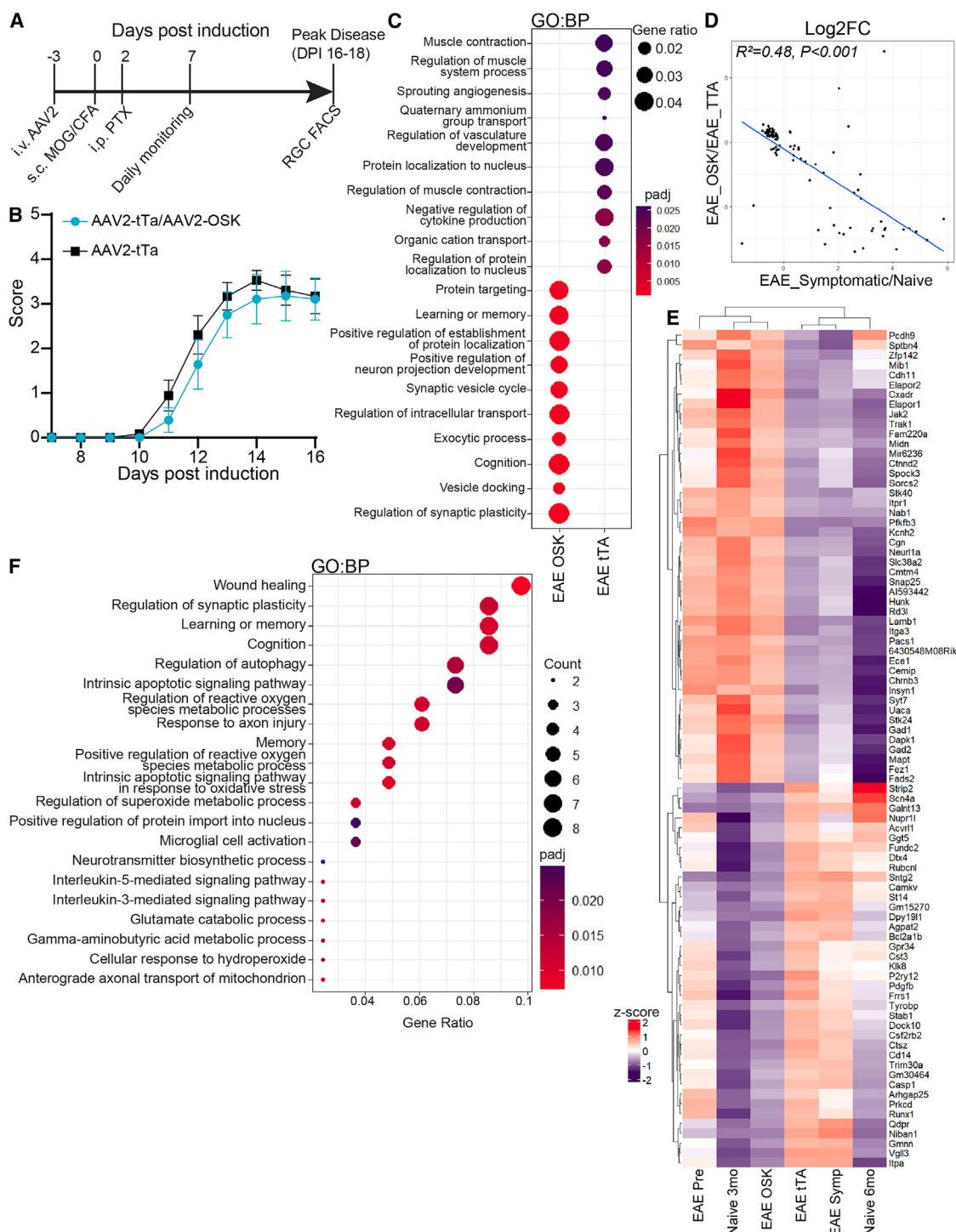


Figure 7. AAV2-OSK mediates gene expression changes in RGCs in EAE

(A) Diagram of experimental timeline showing AAV2-OSK/AAV2-tTa bilateral intravitreal (i.v.) injection 3 days pre-EAE induction (DPI), followed by EAE induction through MOG/CFA subcutaneous (s.c.) injection and pertussis toxin intraperitoneal (PTX i.p.) injection and daily monitoring of EAE score beginning at 7 DPI and continuing until the experiment end.

(B) EAE disease course for animals receiving AAV2-tTa and AAV2-OSK, demonstrating no difference in motor score severity. Error bars: standard error of the mean.

(legend continued on next page)

evidence exists for their senescence.⁶³ Neurons aged *in vitro* and *in vivo* demonstrate accumulation of senescence-associated β -galactosidase activity, DNA damage, and alterations to other senescence-associated proteins.^{54,58} Additionally, loss of nuclear lamina integrity in aged neurons was shown to drive endogenous retrovirus expression, DNA damage, and cellular senescence.⁶⁴ In other neurodegenerative diseases and injury models, markers of senescence in neurons have also been identified.⁶³ For instance, in Alzheimer's disease (AD), the presence of senescent glia and neurons in the CNS is suspected to contribute to impaired memory and cell death.^{65,66} DNA-damage-driven gene fusions are detected in excitatory cortical neurons from patients with AD and suggested to drive differential gene expression in neurons, altering senescence-related pathways.⁶⁷ Similarly, glial and cortical neuron senescence has been reported following traumatic brain injury, where neurons exhibit DNA double-strand breaks, loss of nuclear lamina integrity, and gene expression changes related to senescence processes.^{68–70} Given the growing body of data that a senescent-like phenotype may arise in neurons during aging and in response to various forms of injury and stress,^{71,72} it begs the question whether these characteristics are simply an outcome of accumulated injury over time, overwhelming the neuron's intrinsic repair capacity and impeding its homeostatic functions.

A fascinating piece of the puzzle is the role transcription factors play in promoting neuronal resilience. In our study, we found that the overexpression of three transcription factors involved in cellular rejuvenation (OSK) promoted visual acuity and RGC survival in EAE and diminished the severity of axonal and dendritic pathology. This combination was previously shown to enhance survival and regeneration in RGCs in glaucoma and following optic nerve crush through a Tet1-Tet2 DNA-methylation-dependent mechanism.⁴⁹ Thus, rejuvenated neurons can enact intrinsic injury response programs enabling survival, regeneration, and maintained function. In a glaucoma model, post-injury overexpression of these transcription factors can restore visual function; thus, additional mechanisms, such as synaptic remodeling or compensatory axonal or dendritic remodeling, may also be contributing to the functional improvements seen following rejuvenation. Identifying drug combinations⁷³ and therapies that can engage these programs is an exciting approach. For example, the senomorphomic metformin is currently being investigated for therapeutic potential in MS due to evidence that it may rejuvenate oligodendrocyte precursor cells and promote myelin repair.^{74,75} It is conceivable that this approach may promote a youthful profile in other cell types, thereby exerting off-target beneficial effects. Senolytics, a class of drugs designed to kill senescent cells, are also currently receiving attention for the treatment

of neurodegenerative diseases.⁷⁶ However, if neuronal senescence induces the upregulation of senolytic targets, then these drugs may lead to detrimental outcomes, such as neuronal death. Importantly, treating cellular aging and senescence in MS requires careful consideration of the age of the patients, as it is unique in the neurodegenerative disease field due to its typical onset in young adulthood. MS transitions from a predominantly neuroinflammatory condition in young people (20–30 years of age) to a progressive neurodegenerative disease in older patients, typically between 50 and 60 years of age.^{1,77} Rejuvenating interventions in young patients with relapsing-remitting disease versus in older patients with progressive disease may have differing efficacies in staving off neurodegeneration. Thus, there remain many avenues for investigation into aging and senescence as a therapeutic avenue concerning neurodegenerative diseases, particularly for MS. Approaches incorporating existing immunomodulatory agents, in combination with novel rejuvenating and pro-myelinating therapeutics, may be key to promoting the long-term health of patients in the future.^{44,78}

Limitations of the study

Future studies should assess whether the transduction of AAV-OSK post-EAE induction at peak symptomatology can revert RGC injury measures.⁷⁹ It is likely that significant dendritic reorganization would need to occur to promote functional recovery if AAV-OSK was applied after significant RGC cell loss to compensate for the fewer remaining neurons. This would be interesting to assess in the NOD-EAE model, which evokes a more chronic progressive disease state and may be more amenable to long-term monitoring of visual system function, including by electrophysiological measurements of inner retina function like pattern electroretinography (ERG). Future studies characterizing neuronal-protein-level changes in aging and neuroinflammation to corroborate gene-expression-level changes would benefit the field immensely. Also, our findings are associated strongly with RGCs; different neuron subtypes may demonstrate other unique responses to inflammation and aging. Finally, the impact of sex and gender on neuronal aging in response to inflammation has not been explored and requires further study.

RESOURCE AVAILABILITY

Lead contact

Requests for further information, resources, and reagents should be directed to and will be fulfilled by the lead contact, Alyson E. Fournier (alyson.fournier@mcgill.ca).

Materials availability

This study did not generate new unique reagents.

(C) Top 10 GO BP terms by pathway enrichment analysis in AAV-OSK-transduced EAE RGCs versus control AAV-tTa-transduced EAE RGCs based on significantly dysregulated genes ($p < 0.05$) between groups.

(D) Correlation of the log2FC for genes with $p < 0.05$ in both AAV-OSK versus AAV-tTa and symptomatic EAE versus naive (sequencing data samples are from Figure 2) demonstrates a negative correlation.

(E) Heatmap of all oppositely regulated genes (genes upregulated in AAV-OSK versus AAV-tTa and downregulated in symptomatic EAE versus naive, or vice versa) for sequencing data from EAE presymptomatic, symptomatic, naive 3-month, naive 6-month, EAE-AAV-OSK, and EAE-AAV-tTa.

(F) Pathway analysis of the oppositely regulated genes shown in (E).

Data and code availability

- Data: RNA sequencing and ATAC sequencing data have been deposited at the Gene Expression Omnibus and are publicly available as of the date of publication. All other data reported in this paper will be shared by the [lead contact](#) upon request.
- Code: this paper does not report original code.
- Any additional information required to reanalyze the data reported in this paper is available from the [lead contact](#) upon request.

ACKNOWLEDGMENTS

S.S.D., M.A.H., and A.M.R.G. receive funding from the Canadian Institutes of Health Research (CIHR) Vanier Canada Graduate Scholarship. E.M.-L.H. is funded by the Fonds de Recherche du Québec-Santé Master's Training Scholarship. A.Z. is funded by the Fonds de Recherche du Québec-Santé PhD Training Scholarship and MS Canada. A.E.F. is funded by the CIHR and MS Canada. A.P. holds the T1 Canada Research Chair in MS and is funded by the CIHR, the National MS Society, and the Canadian Foundation for Innovation. D.A.S. is funded by NIH/NIA R01AG019719, a gift from Michael Chambers, and the Glenn Foundation for Medical Research. We would like to acknowledge Dr. Stuart Trenholm for his expertise and support in the 3D printing and building of the optomotor response device and Dr. Kevin Petrecca for helping with patient tissue samples. We would also like to acknowledge the essential technical support from Thomas Stroh and the Montreal Neurological Institute (MNI) Microscopy Core Facility and Julien Sirois and the MNI Flow Cytometry Core Facility.

AUTHOR CONTRIBUTIONS

Conceptualization, S.S.D.; methodology, S.S.D.; investigation, S.S.D., A.M., A.Z., C.G., K.H., A.M.R.G., E.M.-L.H., and M.A.H.; writing – original draft, S.S.D. and A.E.F.; writing – review & editing, S.S.D., Y.R.L., and A.E.F.; funding acquisition, A.E.F.; resources, Y.R.L., D.G., S.Z., A.P., J.A.S., D.A.S., and A.E.F.; data curation, S.S.D., A.M., K.H., and A.Z.; visualization, S.S.D.; supervision, S.S.D. and A.E.F.; project administration, A.E.F.

DECLARATION OF INTERESTS

D.A.S. has equity and consults for Life Biosciences, a company developing rejuvenation medicines. For more information, see <https://sinclair.hms.harvard.edu/david-sinclairs-affiliations>. Y.R.L. holds patents licensed to and minor equity in Life Biosciences.

STAR METHODS

Detailed methods are provided in the online version of this paper and include the following:

- KEY RESOURCES TABLE
- EXPERIMENTAL MODEL AND STUDY PARTICIPANT DETAILS
 - Mouse
 - Human
- METHOD DETAILS
 - Experimental autoimmune encephalomyelitis (EAE)
 - Intraventricular injection of AAV virus
 - Optomotor response
 - Tissue collection
 - Retinal flat-mount immunohistochemistry
 - Retinal cross-section immunohistochemistry
 - Optic nerve cross-section immunohistochemistry
 - Hematoxylin and eosin staining
 - Imaging and analysis
 - Fluorescence-activated cell sorting of RGCs
 - ATAC-sequencing
 - RNA sequencing
 - Gene coexpression analysis
 - Single-cell sequencing data analysis

- Human brain tissue immunohistochemistry
- QUANTIFICATION AND STATISTICAL ANALYSIS

SUPPLEMENTAL INFORMATION

Supplemental information can be found online at <https://doi.org/10.1016/j.celrep.2025.115298>.

Received: November 14, 2023

Revised: October 31, 2024

Accepted: January 21, 2025

Published: February 11, 2025

REFERENCES

1. Filippi, M., Bar-Or, A., Piehl, F., Preziosa, P., Solari, A., Vukusic, S., and Rocca, M.A. (2018). Multiple Sclerosis. *Nat. Rev. Dis. Prim.* 4, 43. <https://doi.org/10.1038/s41572-018-0041-4>.
2. Criste, G., Trapp, B., and Dutta, R. (2014). Axonal loss in multiple sclerosis: causes and mechanisms. *Handb. Clin. Neurol.* 122, 101–113. <https://doi.org/10.1016/B978-0-444-52001-2.00005-4>.
3. Lucichchi, A., Hart, B., Frigerio, I., van Dam, A.M., Perna, L., Offerhaus, H.L., Sty, P.K., Schenk, G.J., and Geurts, J.J.G. (2021). Axon-Myelin Unit Blistering as Early Event in MS Normal Appearing White Matter. *Ann. Neurol.* 89, 711–725. <https://doi.org/10.1002/ana.26014>.
4. Ontaneda, D., and Fox, R.J. (2017). Imaging as an Outcome Measure in Multiple Sclerosis. *Neurotherapeutics* 14, 24–34. <https://doi.org/10.1007/s13311-016-0479-6>.
5. Magliozzi, R., Howell, O.W., Reeves, C., Roncaroli, F., Nicholas, R., Serafini, B., Aloisi, F., and Reynolds, R. (2010). A Gradient of neuronal loss and meningeal inflammation in multiple sclerosis. *Ann. Neurol.* 68, 477–493. <https://doi.org/10.1002/ana.22230>.
6. Mews, I., Bergmann, M., Bunkowski, S., Gullotta, F., and Brück, W. (1998). Oligodendrocyte and axon pathology in clinically silent multiple sclerosis lesions. *Mult. Scler.* 4, 55–62. <https://doi.org/10.1177/135245859800400203>.
7. Bjartmar, C., Kidd, G., Mörk, S., Rudick, R., and Trapp, B.D. (2000). Neurological disability correlates with spinal cord axonal loss and reduced N-acetyl aspartate in chronic multiple sclerosis patients. *Ann. Neurol.* 48, 893–901.
8. Kuhlmann, T., Lingfeld, G., Bitsch, A., Schuchardt, J., and Brück, W. (2002). Acute axonal damage in multiple sclerosis is most extensive in early disease stages and decreases over time. *Brain* 125, 2202–2212. <https://doi.org/10.1093/brain/awf235>.
9. Peterson, J.W., Bö, L., Mörk, S., Chang, A., and Trapp, B.D. (2001). Transsected neurites, apoptotic neurons, and reduced inflammation in cortical multiple sclerosis lesions. *Ann. Neurol.* 50, 389–400. <https://doi.org/10.1002/ana.1123>.
10. Cordano, C., Nourbakhsh, B., Yiu, H.H., Papinutto, N., Caverzasi, E., Abdellah, A., Oertel, F.C., Beaudry-Richard, A., Santaniello, A., Sacco, S., et al. (2022). Differences in Age-related Retinal and Cortical Atrophy Rates in Multiple Sclerosis. *Neurology* 99, e1685–e1693. <https://doi.org/10.1212/WNL.000000000000200977>.
11. Jennings, A.R., and Carroll, W.M. (2015). Oligodendrocyte Lineage Cells in Chronic Demyelination of Multiple Sclerosis Optic Nerve. *Brain Pathol.* 25, 517–530. <https://doi.org/10.1111/bpa.12193>.
12. Riederer, I., Mühlau, M., Hoshi, M.M., Zimmer, C., and Kleine, J.F. (2019). Detecting optic nerve lesions in clinically isolated syndrome and multiple sclerosis: double-inversion recovery magnetic resonance imaging in comparison with visually evoked potentials. *J. Neurol.* 266, 148–156. <https://doi.org/10.1007/s00415-018-9114-2>.
13. Davion, J.B., Lopes, R., Drumez, É., Labreuche, J., Hadhoun, N., Lannoy, J., Vermersch, P., Pruvost, J.P., Leclerc, X., Zéphir, H., and Outterck, O. (2020). Asymptomatic optic nerve lesions: An underestimated cause of

- silent retinal atrophy in MS. *Neurology* 94, e2468–e2478. <https://doi.org/10.1212/wnl.00000000000009504>.
14. London, A., Benhar, I., and Schwartz, M. (2013). The retina as a window to the brain—from eye research to CNS disorders. *Nat. Rev. Neurosci.* 9, 44–53. <https://doi.org/10.1038/nrneurol.2012.227>.
 15. Ngamsombat, C., Tian, Q., Fan, Q., Russo, A., Machado, N., Polackal, M., George, I.C., Witzel, T., Klawiter, E.C., and Huang, S.Y. (2020). Axonal damage in the optic radiation assessed by white matter tract integrity metrics is associated with retinal thinning in multiple sclerosis. *Neuroimage. Clin.* 27, 102293. <https://doi.org/10.1016/j.nicl.2020.102293>.
 16. You, Y., Barnett, M.H., Yiannikas, C., Parratt, J.D.E., Matthews, J.G., Graham, S.L., and Klistorner, A. (2021). Interferon-β Is Less Effective Than Other Drugs in Controlling the Rate of Retinal Ganglion Cell Loss in MS. *Neurol. Neuroimmunol. Neuroinflamm.* 8, e971. <https://doi.org/10.1212/nxi.0000000000000971>.
 17. Rohowitz, L.J., Vu, Q., Ablabutyan, L., Gratton, S.M., Kunjukunju, N., Wallace, B.S., and Koulen, P. (2020). Microperimetry as a diagnostic tool for the detection of early, subclinical retinal damage and visual impairment in multiple sclerosis. *BMC Ophthalmol.* 20, 367. <https://doi.org/10.1186/s12886-020-01620-9>.
 18. Dreyer-Alster, S., Gal, A., and Achiron, A. (2022). Optical Coherence Tomography Is Associated With Cognitive Impairment in Multiple Sclerosis. *J. Neuro Ophthalmol.* 42, e14–e21. <https://doi.org/10.1097/wno.0000000000001326>.
 19. Garcia-Martin, E., Ara, J.R., Martin, J., Almarcegui, C., Dolz, I., Vilades, E., Gil-Arribas, L., Fernandez, F.J., Polo, V., Larrosa, J.M., et al. (2017). Retinal and Optic Nerve Degeneration in Patients with Multiple Sclerosis Followed up for 5 Years. *Ophthalmology* 124, 688–696. <https://doi.org/10.1016/j.ophtha.2017.01.005>.
 20. Rothman, A., Murphy, O.C., Fitzgerald, K.C., Button, J., Gordon-Lipkin, E., Ratchford, J.N., Newsome, S.D., Mowry, E.M., Sotirchos, E.S., Syc-Mazurek, S.B., et al. (2019). Retinal measurements predict 10-year disability in multiple sclerosis. *Ann. Clin. Transl. Neurol.* 6, 222–232. <https://doi.org/10.1002/acn3.674>.
 21. Glasner, P., Sabisz, A., Chylińska, M., Komendziński, J., Wyszomirska, A., and Karaszewski, B. (2022). Retinal nerve fiber and ganglion cell complex layer thicknesses mirror brain atrophy in patients with relapsing-remitting multiple sclerosis. *Restor. Neurol. Neurosci.* 40, 35–42. <https://doi.org/10.3233/rnn-211176>.
 22. Drake, S.S., Charabati, M., Simas, T., Xu, Y.K.T., Maes, E.J.P., Shi, S.S., Antel, J., Prat, A., Morquette, B., and Fournier, A.E. (2022). 3-Dimensional Immunostaining and Automated Deep-Learning Based Analysis of Nerve Degeneration. *Int. J. Mol. Sci.* 23, 14811. <https://doi.org/10.3390/ijms232314811>.
 23. Fernández Blanco, L., Marzin, M., Leistra, A., van der Valk, P., Nutma, E., and Amor, S. (2022). Immunopathology of the optic nerve in multiple sclerosis. *Clin. Exp. Immunol.* 209, 236–246. <https://doi.org/10.1093/cei/uxac063>.
 24. Jin, J., Smith, M.D., Kersbergen, C.J., Kam, T.I., Viswanathan, M., Martin, K., Dawson, T.M., Dawson, V.L., Zack, D.J., Whartenby, K., and Calabresi, P.A. (2019). Glial pathology and retinal neurotoxicity in the anterior visual pathway in experimental autoimmune encephalomyelitis. *Acta Neuropathol. Commun.* 7, 125. <https://doi.org/10.1186/s40478-019-0767-6>.
 25. Horstmann, L., Kuehn, S., Pedreiruria, X., Haak, K., Pfarrer, C., Dick, H.B., Kleiter, I., and Joachim, S.C. (2016). Microglia response in retina and optic nerve in chronic experimental autoimmune encephalomyelitis. *J. Neuroimmunol.* 298, 32–41. <https://doi.org/10.1016/j.jneuroim.2016.06.008>.
 26. Cruz-Herranz, A., Dietrich, M., Hilla, A.M., Yiu, H.H., Levin, M.H., Hecker, C., Issberner, A., Hallenberger, A., Cordano, C., Lehmann-Horn, K., et al. (2019). Monitoring retinal changes with optical coherence tomography predicts neuronal loss in experimental autoimmune encephalomyelitis. *J. Neuroinflammation* 16, 203. <https://doi.org/10.1186/s12974-019-1583-4>.
 27. Manogaran, P., Samardzija, M., Schad, A.N., Wicki, C.A., Walker-Egger, C., Rudin, M., Grimm, C., and Schippling, S. (2019). Retinal pathology in experimental optic neuritis is characterized by retrograde degeneration and gliosis. *Acta Neuropathol. Commun.* 7, 116. <https://doi.org/10.1186/s40478-019-0768-5>.
 28. Nishioka, C., Liang, H.F., Barsamian, B., and Sun, S.W. (2019). Sequential phases of RGC axonal and somatic injury in EAE mice examined using DTI and OCT. *Mult. Scler. Relat. Disord.* 27, 315–323. <https://doi.org/10.1016/j.msard.2018.11.010>.
 29. Morquette, B., Južwik, C.A., Drake, S.S., Charabati, M., Zhang, Y., Lé-cuyer, M.A., Galloway, D.A., Dumas, A., de Faria Junior, O., Paradis-Isler, N., et al. (2019). MicroRNA-223 protects neurons from degeneration in experimental autoimmune encephalomyelitis. *Brain* 142, 2979–2995. <https://doi.org/10.1093/brain/awz245>.
 30. Gonsette, R.E. (2008). Neurodegeneration in multiple sclerosis: the role of oxidative stress and excitotoxicity. *J. Neurol. Sci.* 274, 48–53. <https://doi.org/10.1016/j.jns.2008.06.029>.
 31. Lassmann, H. (2010). Axonal and neuronal pathology in multiple sclerosis: What have we learnt from animal models. *Exp. Neurol.* 225, 2–8. <https://doi.org/10.1016/j.expneurol.2009.10.009>.
 32. Mahad, D.H., Trapp, B.D., and Lassmann, H. (2015). Pathological mechanisms in progressive multiple sclerosis. *Lancet Neurol.* 14, 183–193. [https://doi.org/10.1016/s1474-4422\(14\)70256-x](https://doi.org/10.1016/s1474-4422(14)70256-x).
 33. Werner, P., Pitt, D., and Raine, C.S. (2000). Glutamate excitotoxicity—a mechanism for axonal damage and oligodendrocyte death in Multiple Sclerosis? In *Advances in Research on Neurodegeneration*, P. Riederer, D.B. Calne, R. Horowski, Y. Mizuno, C.W. Olanow, W. Poewe, and M.B.H. Youdim, eds. (Springer), pp. 375–385. https://doi.org/10.1007/978-3-7091-6301-6_27.
 34. Yong, V.W. (2022). Microglia in multiple sclerosis: Protectors turn destroyers. *Neuron* 110, 3534–3548. <https://doi.org/10.1016/j.neuron.2022.06.023>.
 35. Kular, L., Klose, D., Urdánoz-Casado, A., Ewing, E., Planell, N., Gomez-Cabrero, D., Needhamson, M., and Jagodic, M. (2022). Epigenetic clock indicates accelerated aging in glial cells of progressive multiple sclerosis patients. *Front. Aging Neurosci.* 14, 926468. <https://doi.org/10.3389/fragi.2022.926468>.
 36. Maltby, V., Xavier, A., Ewing, E., Campagna, M.P., Sampangi, S., Scott, R.J., Butzkueven, H., Jokubaitis, V., Kular, L., Bos, S., et al. (2023). Evaluation of Cell-Specific Epigenetic Age Acceleration in People With Multiple Sclerosis. *Neurology* 101, e679–e689. <https://doi.org/10.1212/wnl.000000000000207489>.
 37. Krysko, K.M., Henry, R.G., Cree, B.A.C., Lin, J., University of California San Francisco MS-EPIC Team; Caillier, S., Santaniello, A., Zhao, C., Gomez, R., and Bevan, C. (2019). Telomere Length Is Associated with Disability Progression in Multiple Sclerosis. *Ann. Neurol.* 86, 671–682. <https://doi.org/10.1002/ana.25592>.
 38. Bühring, J., Hecker, M., Fitzner, B., and Zettl, U.K. (2021). Systematic Review of Studies on Telomere Length in Patients with Multiple Sclerosis. *Aging Dis.* 12, 1272–1286. <https://doi.org/10.14336/ad.2021.0106>.
 39. Zhang, Y., Atkinson, J., Burd, C.E., Graves, J., and Segal, B.M. (2023). Biological aging in multiple sclerosis. *Mult. Scler.* 29, 1701–1708. <https://doi.org/10.1177/13524585231204122>.
 40. Atkinson, J.R., Jerome, A.D., Sas, A.R., Munie, A., Wang, C., Ma, A., Arnold, W.D., and Segal, B.M. (2022). Biological aging of CNS-resident cells alters the clinical course and immunopathology of autoimmune demyelinating disease. *JCI Insight* 7, e158153. <https://doi.org/10.1172/jci.insight.158153>.
 41. López-Otín, C., Blasco, M.A., Partridge, L., Serrano, M., and Kroemer, G. (2023). Hallmarks of aging: An expanding universe. *Cell* 186, 243–278. <https://doi.org/10.1016/j.cell.2022.11.001>.

42. Kuehnemann, C., and Wiley, C.D. (2024). Senescent cells at the crossroads of aging, disease, and tissue homeostasis. *Aging Cell* 23, e13988. <https://doi.org/10.1111/acel.13988>.
43. Gurkar, A.U., Gerencser, A.A., Mora, A.L., Nelson, A.C., Zhang, A.R., Lagando, A.B., Enninfoul, A., Benz, C., Furman, D., Beaulieu, D., et al. (2023). Spatial mapping of cellular senescence: emerging challenges and opportunities. *Nat. Aging* 3, 776–790. <https://doi.org/10.1038/s43587-023-00446-6>.
44. Sutter, P.A., McKenna, M.G., Imitola, J., Pijewski, R.S., and Crocker, S.J. (2022). Therapeutic opportunities for targeting cellular senescence in progressive multiple sclerosis. *Curr. Opin. Pharmacol.* 63, 102184. <https://doi.org/10.1016/j.coph.2022.102184>.
45. Drake, S.S., Zaman, A., Simas, T., and Fournier, A.E. (2023). Comparing RNA-sequencing datasets from astrocytes, oligodendrocytes, and microglia in multiple sclerosis identifies novel dysregulated genes relevant to inflammation and myelination. *WIREs Mech. Dis.* 15, e1594. <https://doi.org/10.1002/wsbm.1594>.
46. Schirmer, L., Velmeshev, D., Holmqvist, S., Kaufmann, M., Werneburg, S., Jung, D., Vistnes, S., Stockley, J.H., Young, A., Steindel, M., et al. (2019). Neuronal vulnerability and multilineage diversity in multiple sclerosis. *Nature* 573, 75–82. <https://doi.org/10.1038/s41586-019-1404-z>.
47. Juźwik, C.A., Drake, S., Lécuyer, M.A., Johnson, R.M., Morquette, B., Zhang, Y., Charabati, M., Sagan, S.M., Bar-Or, A., Prat, A., and Fournier, A.E. (2018). Neuronal microRNA regulation in Experimental Autoimmune Encephalomyelitis. *Sci. Rep.* 8, 13437. <https://doi.org/10.1038/s41598-018-31542-y>.
48. Schattling, B., Engler, J.B., Volkmann, C., Rothammer, N., Woo, M.S., Petersen, M., Winkler, I., Kaufmann, M., Rosenkranz, S.C., Fejtova, A., et al. (2019). Bassoon proteinopathy drives neurodegeneration in multiple sclerosis. *Nat. Neurosci.* 22, 887–896. <https://doi.org/10.1038/s41593-019-0385-4>.
49. Lu, Y., Brommer, B., Tian, X., Krishnan, A., Meer, M., Wang, C., Vera, D.L., Zeng, Q., Yu, D., Bonkowski, M.S., et al. (2020). Reprogramming to recover youthful epigenetic information and restore vision. *Nature* 588, 124–129. <https://doi.org/10.1038/s41586-020-2975-4>.
50. Duffy, M.F., Ding, J., Langston, R.G., Shah, S.I., Nalls, M.A., Scholz, S.W., Whitaker, D.T., Auluck, P.K., Marenco, S., Gibbs, J.R., and Cookson, M.R. (2023). Divergent patterns of healthy aging across human brain regions at single-cell resolution reveal links to neurodegenerative disease. Preprint at bioRxiv. <https://doi.org/10.1101/2023.07.31.551097>.
51. Hahn, O., Foltz, A.G., Atkins, M., Kedir, B., Moran-Losada, P., Guldner, I.H., Munson, C., Kern, F., Pálovics, R., Lu, N., et al. (2023). Atlas of the aging mouse brain reveals white matter as vulnerable foci. *Cell* 186, 4117–4133.e22. <https://doi.org/10.1016/j.cell.2023.07.027>.
52. Ximerakis, M., Holton, K.M., Giadone, R.M., Ozek, C., Saxena, M., Santiago, S., Adiconis, X., Dionne, D., Nguyen, L., Shah, K.M., et al. (2023). Heterochronic parabiosis reprograms the mouse brain transcriptome by shifting aging signatures in multiple cell types. *Nat. Aging* 3, 327–345. <https://doi.org/10.1038/s43587-023-00373-6>.
53. Baker, D.J., and Petersen, R.C. (2018). Cellular senescence in brain aging and neurodegenerative diseases: evidence and perspectives. *J. Clin. Invest.* 128, 1208–1216. <https://doi.org/10.1172/jci95145>.
54. Moreno-Blas, D., Gorostieta-Salas, E., Pommer-Alba, A., Muciño-Hernández, G., Gerónimo-Olvera, C., Maciel-Barón, L.A., Konigsberg, M., Massieu, L., and Castro-Obregón, S. (2019). Cortical neurons develop a senescence-like phenotype promoted by dysfunctional autophagy. *Aging (Albany NY)* 11, 6175–6198. <https://doi.org/10.18632/aging.102181>.
55. Saul, D., Kosinsky, R.L., Atkinson, E.J., Doolittle, M.L., Zhang, X., LeBras-seeur, N.K., Pignolo, R.J., Robbins, P.D., Niedernhofer, L.J., Ikeno, Y., et al. (2022). A new gene set identifies senescent cells and predicts senescence-associated pathways across tissues. *Nat. Commun.* 13, 4827. <https://doi.org/10.1038/s41467-022-32552-1>.
56. Zindler, E., and Zipp, F. (2010). Neuronal injury in chronic CNS inflammation. *Best Pract. Res. Clin. Anaesthesiol.* 24, 551–562. <https://doi.org/10.1016/j.bpa.2010.11.001>.
57. Kaufmann, M., Schaupp, A.-L., Sun, R., Coscia, F., Dendrou, C.A., Cortes, A., Kaur, G., Evans, H.G., Mollbrink, A., Navarro, J.F., et al. (2022). Identification of early neurodegenerative pathways in progressive multiple sclerosis. *Nat. Neurosci.* 25, 944–955. <https://doi.org/10.1038/s41593-022-01097-3>.
58. Jurk, D., Wang, C., Miwa, S., Maddick, M., Korolchuk, V., Tsolou, A., Gonos, E.S., Thrasivoulou, C., Saffrey, M.J., Cameron, K., and von Zglinicki, T. (2012). Postmitotic neurons develop a p21-dependent senescence-like phenotype driven by a DNA damage response. *Aging Cell* 11, 996–1004. <https://doi.org/10.1111/j.1474-9726.2012.00870.x>.
59. Dyer, M., Phipps, A.J., Mitew, S., Taberlay, P.C., and Woodhouse, A. (2019). Age, but Not Amyloidosis, Induced Changes in Global Levels of Histone Modifications in Susceptible and Disease-Resistant Neurons in Alzheimer's Disease Model Mice. *Front. Aging Neurosci.* 11, 68. <https://doi.org/10.3389/fnagi.2019.00068>.
60. Dou, Z., Xu, C., Donahue, G., Shimi, T., Pan, J.-A., Zhu, J., Ivanov, A., Capell, B.C., Drake, A.M., Shah, P.P., et al. (2015). Autophagy mediates degradation of nuclear lamina. *Nature* 527, 105–109. <https://doi.org/10.1038/nature15548>.
61. Freund, A., Laberge, R.M., Demaria, M., and Campisi, J. (2012). Lamin B1 loss is a senescence-associated biomarker. *Mol. Biol. Cell* 23, 2066–2075. <https://doi.org/10.1091/mbc.E11-10-0884>.
62. Sun, S., Li, J., Wang, S., Li, J., Ren, J., Bao, Z., Sun, L., Ma, X., Zheng, F., Ma, S., et al. (2023). CHIT1-positive microglia drive motor neuron ageing in the primate spinal cord. *Nature* 624, 611–620. <https://doi.org/10.1038/s41586-023-06783-1>.
63. Sah, E., Krishnamurthy, S., Ahmidouch, M.Y., Gillispie, G.J., Milligan, C., and Orr, M.E. (2021). The Cellular Senescence Stress Response in Post-Mitotic Brain Cells: Cell Survival at the Expense of Tissue Degeneration. *Life* 11, 229. <https://doi.org/10.3390/life11030229>.
64. Zhang, H., Li, J., Yu, Y., Ren, J., Liu, Q., Bao, Z., Sun, S., Liu, X., Ma, S., Liu, Z., et al. (2023). Nuclear lamina erosion-induced resurrection of endogenous retroviruses underlies neuronal aging. *Cell Rep.* 42, 112593. <https://doi.org/10.1016/j.celrep.2023.112593>.
65. Herdy, J.R., Traxler, L., Agarwal, R.K., Karbacher, L., Schlachetzki, J.C.M., Boehnke, L., Zangwill, D., Galasko, D., Glass, C.K., Mertens, J., and Gage, F.H. (2022). Increased post-mitotic senescence in aged human neurons is a pathological feature of Alzheimer's disease. *Cell Stem Cell* 29, 1637–1652.e6. <https://doi.org/10.1016/j.stem.2022.11.010>.
66. Bussian, T.J., Aziz, A., Meyer, C.F., Swenson, B.L., van Deursen, J.M., and Baker, D.J. (2018). Clearance of senescent glial cells prevents tau-dependent pathology and cognitive decline. *Nature* 562, 578–582. <https://doi.org/10.1038/s41586-018-0543-y>.
67. Dileep, V., Boix, C.A., Mathys, H., Marco, A., Welch, G.M., Meharena, H.S., Loon, A., Jeloka, R., Peng, Z., Bennett, D.A., et al. (2023). Neuronal DNA double-strand breaks lead to genome structural variations and 3D genome disruption in neurodegeneration. *Cell* 186, 4404–4421.e20. <https://doi.org/10.1016/j.cell.2023.08.038>.
68. Schwab, N., Grenier, K., and Hazrati, L.N. (2019). DNA repair deficiency and senescence in concussed professional athletes involved in contact sports. *Acta Neuropathol. Commun.* 7, 182. <https://doi.org/10.1186/s40478-019-0822-3>.
69. Schwab, N., Ju, Y., and Hazrati, L.N. (2021). Early onset senescence and cognitive impairment in a murine model of repeated mTBI. *Acta Neuropathol. Commun.* 9, 82. <https://doi.org/10.1186/s40478-021-01190-x>.
70. Schwab, N., Taskina, D., Leung, E., Innes, B.T., Bader, G.D., and Hazrati, L.N. (2022). Neurons and glial cells acquire a senescent signature after repeated mild traumatic brain injury in a sex-dependent manner. *Front. Neurosci.* 16, 1027116. <https://doi.org/10.3389/fnins.2022.1027116>.

71. Rizzo, J.F., 3rd, Shah, M.P., Krasniqi, D., Lu, Y.R., Sinclair, D.A., and Ksander, B.R. (2024). The Role of Epigenetics in Accelerated Aging: A Reconsideration of Later-Life Visual Loss After Early Optic Neuropathy. *J. Neuro Ophthalmol.* 44, 16–21. <https://doi.org/10.1097/wno.0000000000002041>.
72. Xu, Q., Rydz, C., Nguyen Huu, V.A., Rocha, L., Palomino La Torre, C., Lee, I., Cho, W., Jabari, M., Donello, J., Lyon, D.C., et al. (2022). Stress induced aging in mouse eye. *Aging Cell* 21, e13737. <https://doi.org/10.1111/ace.13737>.
73. Yang, J.H., Petty, C.A., Dixon-McDougall, T., Lopez, M.V., Tyshkovskiy, A., Maybury-Lewis, S., Tian, X., Ibrahim, N., Chen, Z., Griffin, P.T., et al. (2023). Chemically induced reprogramming to reverse cellular aging. *Aging (Albany NY)* 15, 5966–5989. <https://doi.org/10.18632/aging.204896>.
74. Dziedzic, A., Saluk-Bijak, J., Miller, E., and Bijak, M. (2020). Metformin as a Potential Agent in the Treatment of Multiple Sclerosis. *Int. J. Mol. Sci.* 21, 5957. <https://doi.org/10.3390/ijms21175957>.
75. Neumann, B., Baror, R., Zhao, C., Segel, M., Dietmann, S., Rawji, K.S., Foerster, S., McClain, C.R., Chalut, K., van Wijngaarden, P., and Franklin, R.J.M. (2019). Metformin Restores CNS Remyelination Capacity by Rejuvenating Aged Stem Cells. *Cell Stem Cell* 25, 473–485.e8. <https://doi.org/10.1016/j.stem.2019.08.015>.
76. Sahu, M.R., Rani, L., Subba, R., and Mondal, A.C. (2022). Cellular senescence in the aging brain: A promising target for neurodegenerative diseases. *Mech. Ageing Dev.* 204, 111675. <https://doi.org/10.1016/j.mad.2022.111675>.
77. Kuhlmann, T., Moccia, M., Coetzee, T., Cohen, J.A., Correale, J., Graves, J., Marrie, R.A., Montalban, X., Yong, V.W., Thompson, A.J., et al. (2023). Multiple sclerosis progression: time for a new mechanism-driven framework. *Lancet Neurol.* 22, 78–88. [https://doi.org/10.1016/S1474-4422\(22\)00289-7](https://doi.org/10.1016/S1474-4422(22)00289-7).
78. Cunniffe, N., Vuong, K.A., Ainslie, D., Baker, D., Beveridge, J., Bickley, S., Camilleri, P., Craner, M., Fitzgerald, D., de la Fuente, A.G., et al. (2021). Systematic approach to selecting licensed drugs for repurposing in the treatment of progressive multiple sclerosis. *J. Neurol. Neurosurg. Psychiatry* 92, 295–302. <https://doi.org/10.1136/jnnp-2020-324286>.
79. Karg, M.M., Lu, Y.R., Refaian, N., Cameron, J., Hoffmann, E., Hoppe, C., Shirahama, S., Shah, M., Krasniqi, D., Krishnan, A., et al. (2023). Sustained Vision Recovery by OSK Gene Therapy in a Mouse Model of Glaucoma. *Cell. Reprogr.* 25, 288–299. <https://doi.org/10.1089/cell.2023.0074>.
80. Wu, T., Hu, E., Xu, S., Chen, M., Guo, P., Dai, Z., Feng, T., Zhou, L., Tang, W., Zhan, L., et al. (2021). clusterProfiler 4.0: A universal enrichment tool for interpreting omics data. *Innovation* 2, 100141. <https://doi.org/10.1016/j.xinn.2021.100141>.
81. Li, C., Deans, N.C., and Buell, C.R. (2023). "Simple Tidy GeneCoEx": A gene co-expression analysis workflow powered by tidyverse and graph-based clustering in R. *Plant Genome* 16, e20323. <https://doi.org/10.1002/tpg2.20323>.
82. Hänzelmann, S., Castelo, R., and Guinney, J. (2013). GSVA: gene set variation analysis for microarray and RNA-seq data. *BMC Bioinf.* 14, 1–15. <https://doi.org/10.1186/1471-2105-14-7>.
83. Kim, D., Paggi, J.M., Park, C., Bennett, C., and Salzberg, S.L. (2019). Graph-based genome alignment and genotyping with HISAT2 and HISAT-genotype. *Nat. Biotechnol.* 37, 907–915. <https://doi.org/10.1038/s41587-019-0201-4>.
84. Anders, S., Pyl, P.T., and Huber, W. (2015). HTSeq—a Python framework to work with high-throughput sequencing data. *Bioinformatics* 31, 166–169. <https://doi.org/10.1093/bioinformatics/btu638>.
85. Martin, M. (2011). Cutadapt removes adapter sequences from high-throughput sequencing reads. *EMBnet J.* 17, 10–12. <https://doi.org/10.14806/ej.17.1.200>.
86. Bolger, A.M., Lohse, M., and Usadel, B. (2014). Trimmomatic: a flexible trimmer for Illumina sequence data. *Bioinformatics* 30, 2114–2120. <https://doi.org/10.1093/bioinformatics/btu170>.
87. Langmead, B., and Salzberg, S.L. (2012). Fast gapped-read alignment with Bowtie 2. *Nat. Methods* 9, 357–359. <https://doi.org/10.1038/nmeth.1923>.
88. Younesy, H., Möller, T., Lorincz, M.C., Karimi, M.M., and Jones, S.J.M. (2015). VisRseq: R-based visual framework for analysis of sequencing data. *BMC Bioinf.* 16, S2. <https://doi.org/10.1186/1471-2105-16-S11-S2>.
89. Schindelin, J., Arganda-Carreras, I., Frise, E., Kaynig, V., Longair, M., Pietzsch, T., Preibisch, S., Rueden, C., Saalfeld, S., Schmid, B., et al. (2012). Fiji: an open-source platform for biological-image analysis. *Nat. Methods* 9, 676–682. <https://doi.org/10.1038/nmeth.2019>.
90. Satija, R., Farrell, J.A., Gennert, D., Schier, A.F., and Regev, A. (2015). Spatial reconstruction of single-cell gene expression data. *Nat. Biotechnol.* 33, 495–502. <https://doi.org/10.1038/nbt.3192>.
91. Polman, C.H., Reingold, S.C., Banwell, B., Clanet, M., Cohen, J.A., Filippi, M., Fujihara, K., Havrdova, E., Hutchinson, M., Kappos, L., et al. (2011). Diagnostic criteria for multiple sclerosis: 2010 revisions to the McDonald criteria. *Ann. Neurol.* 69, 292–302. <https://doi.org/10.1002/ana.22366>.
92. Caves, E.M., Troscianko, J., and Kelley, L.A. (2020). A customizable, low-cost optomotor apparatus: A powerful tool for behaviourally measuring visual capability. *Methods Ecol. Evol.* 11, 1319–1324. <https://doi.org/10.1111/2041-210X.13449>.
93. Hao, Y., Hao, S., Andersen-Nissen, E., Mauck, W.M., 3rd, Zheng, S., Butler, A., Lee, M.J., Wilk, A.J., Darby, C., Zager, M., et al. (2021). Integrated analysis of multimodal single-cell data. *Cell* 184, 3573–3587.e29. <https://doi.org/10.1016/j.cell.2021.04.048>.
94. Kuhlmann, T., Ludwin, S., Prat, A., Antel, J., Brück, W., and Lassmann, H. (2017). An updated histological classification system for multiple sclerosis lesions. *Acta Neuropathol.* 133, 13–24. <https://doi.org/10.1007/s00401-016-1653-y>.
95. Dhaeze, T., Tremblay, L., Lachance, C., Peelen, E., Zandee, S., Grasmuck, C., Bourbonnière, L., Larouche, S., Ayrignac, X., Rébillard, R.M., et al. (2019). CD70 defines a subset of proinflammatory and CNS-pathogenic TH1/TH17 lymphocytes and is overexpressed in multiple sclerosis. *Cell. Mol. Immunol.* 16, 652–665. <https://doi.org/10.1038/s41423-018-0198-5>.
96. Broux, B., Zandee, S., Gowing, E., Charabati, M., Lécuyer, M.A., Tastet, O., Hachehouche, L., Bourbonnière, L., Ouimet, J.P., Lemaitre, F., et al. (2020). Interleukin-26, preferentially produced by TH17 lymphocytes, regulates CNS barrier function. *Neuro. Neuroimmunol. Neuroinflamm.* 7, e870. <https://doi.org/10.1212/nxi.0000000000000870>.

STAR★METHODS

KEY RESOURCES TABLE

REAGENT or RESOURCE	SOURCE	IDENTIFIER
Antibodies		
SMI32	Biolegend	Cat# 801702; RRID:AB_2715852
BRN3A	Millipore sigma	Cat# MAB1585; RRID:AB_94166
yH2AX	Millipore sigma; Abcam	Cat# 05-636; RRID:AB_309864; Cat# ab11174; RRID:AB_297813
LAMINB1	Abcam	Cat# ab16048; RRID:AB_443298
H3K27me3	Cell signaling	Cat# 9733; RRID:AB_2616029
MAP2	Abcam	Cat# ab5392; RRID:AB_2138153
RBPM5	Phosphosolutions	Cat# 1830-RBPM5; RRID:AB_2492225
GFP	Abcam	Cat# ab13970; RRID:AB_300798
KLF4	Rnd systems	Cat# AF3158; RRID:AB_2130245
CD90.2	Thermofisher	Cat# 17-0902-82; RRID:AB_469422
NEUN	Abcam	Cat# ab279297; RRID:AB_3095692
CD16/32	Biolegend	Cat# 101301; RRID:AB_312800
Bacterial and virus strains		
AAV2-TRE-d2EGFP	Lu et al. ⁴⁹	N/A
AAV2-CMV-tTa	Lu et al. ⁴⁹	N/A
AAV2-TRE-OSK	Lu et al. ⁴⁹	N/A
Biological samples		
Cortical tissue sections collected during surgical resectioning from patients with frontotemporal brain tumors	This paper	N/A
Cortical tissue sections collected during autopsy from patients with MS	This paper	N/A
Chemicals, peptides, and recombinant proteins		
Myelin oligodendrocyte protein	Alpha Diagnostic	MOG3555-P-5
Incomplete Freund's adjuvant	DIFCO	DF639-60-6
Killed mycobacterium tuberculosis	DIFCO	DF3114-33-8
Pertussis toxin	Cedarlane	19546-50
Critical commercial assays		
H&E Staining Kit	Abcam	ab245880
Papain Dissociation System	Worthington	LK003150
Zombie Aqua	Biolegend	423101
Nextera DNA library prep kit	Illumina	15028212
miRNeasy Mini Kit	Qiagen	217004
Deposited data		
FACS enriched RGC RNA-sequencing data from naive and EAE mice	This paper	GEO: GSE247173
FACS enriched RGC ATAC-sequencing data from naive and EAE mice	This paper	GEO: GSE246702
FACS enriched RGC RNA-sequencing data from 5 month to 12 month old mice	Lu et al. ⁴⁹	NCBI BioProject: PRJNA655981
Single nucleus sequencing from cortical gray matter of patients with MS	Schirmer et al. ⁴⁶	NCBI BioProject: PRJNA544731
TRAP-seq from EAE motor neurons and naive mice	Schattling et al. ⁴⁸	NCBI BioProject: PRJNA414103

(Continued on next page)

Continued

REAGENT or RESOURCE	SOURCE	IDENTIFIER
Experimental models: Organisms/strains		
Mouse: B6.Cg-Tg(Thy1-EYFP)15Jrs/J (Thy1-STOP-YFP)	Jackson Labs	IMSR_JAX:005630
Mouse: Slc17a6tm2(cre)Lowl/J (vGlut2-Cre)	Jackson Labs	IMSR_JAX:016963
Software and algorithms		
ClusterProfiler	Wu et al. ⁸⁰	https://yulab-smu.top/biomedical-knowledge-mining-book
Simple Tidy Gene Coexpression	Li et al. ⁸¹	https://github.com/cxli233/SimpleTidy_GeneCoEx
GSVA	Hanzelmann et al. ⁸²	https://www.bioconductor.org/packages/release/bioc/vignettes/GSVA
Hisat2	Kim et al. ⁸³	https://daehwankimlab.github.io/Hisat2/
Htseq	Anders et al. ⁸⁴	https://htseq.readthedocs.io/en/latest/
Cutadapt	Martin ⁸⁵	https://cutadapt.readthedocs.io/en/stable/
Trimmomatic	Bolger et al. ⁸⁶	https://github.com/timflutre/trimmmatic
Bowtie2	Langmead et al. ⁸⁷	https://bowtie-bio.sourceforge.net/bowtie2/index.shtml
VisR	Younesy et al. ⁸⁸	https://visrsoftware.github.io/
FIJI	Schindelin et al. ⁸⁹	https://imagej.net
Seurat	Satija et al. ⁹⁰	https://satijalab.org/seurat/

EXPERIMENTAL MODEL AND STUDY PARTICIPANT DETAILS

Mouse

All mouse experiments were performed according to the guidelines set by the Canadian Council on Animal Care (CCAC), as approved and overseen by the Neuro Animal Care Committee (Montreal Neurological Institute) and the McGill Animal Compliance Office (Protocol Fournier-4748). Mice were housed and maintained under standard husbandry and housing conditions. Transgenic mice were maintained as homozygous crosses between B6.Cg-Tg(Thy1-EYFP)15Jrs/J (Thy1-STOP-YFP) and Slc17a6tm2(cre)Lowl/J (vGlut2-Cre) strains, and used in EAE experiments between 7 and 8 weeks of age. Female mice were used for EAE experiments.

Human

Healthy control brain tissue was obtained from the resection path during frontotemporal brain tumor neurosurgery (sample size $n = 2$) and MS tissue (sample size $n = 3$) was collected during autopsy from patients diagnosed with clinical and neuropathological MS according to the revised 2010 McDonald's criteria.⁹¹ All tissue samples were collected from patients with full ethical approval and informed consent as approved by the MUHC Research Ethics Board (Protocols: BH07.001, Nagano 20.332-YP, Stratton 2020-6185, and Stratton 2021-7215).

METHOD DETAILS

Experimental autoimmune encephalomyelitis (EAE)

EAE was induced 7–8-week-old female mice as described previously.²⁹ Briefly, myelin oligodendrocyte protein (MOG) was prepared in an emulsion of complete Freund's adjuvant (CFA) and 100 μ L was injected subcutaneously. Two days later, animals were injected intraperitoneally with 400 ng pertussis toxin in 200 μ L sterile Hank's Balanced Salt Solution (HBSS). Animals were monitored for up to three weeks post induction for weight loss and motor symptom development. Motor symptoms were scored on a scale of 0–5, representing symptoms of ascending motor paralysis. All scoring was conducted blinded to treatment condition.

Intravitreal injection of AAV virus

Bilateral intravitreal injections were performed three days prior to EAE induction. Briefly, mice were anesthetized with isoflurane, and the eye was treated with topical anesthetic for pain management during and after the procedure. Suture thread was used to pull back the eyelid and pull the conjunctiva to rotate the eye forward. A window was cut through the conjunctiva to visualize the injection location, then a microneedle was used to pierce the globe of the eye and inject the solution. The needle was held in place for 30 s to ensure mixing of the injected solution with the vitreous liquid, then the needle and suture thread were removed, and the mouse was

monitored for recovery. 2 μ L of virus mixture of AAV2-TRE-d2EGFP/AAV2-CMV-tTA or AAV2-TRE-OSK/AAV2-CMV-tTA was injected per eye. For animals used for RGC FACS and RNA-sequencing, AAV2-TRE-OSK/AAV2-CMV-tTA (AAV-OSK condition) or aAV2-CMV-tTA (AAV-tTA control condition) was injected in each eye.

Optomotor response

Optomotor response was tested in a custom-built drum with striped paper sheets rotated around the animal at 2 rpm in standard lighting.⁹² Stripe sizes tested included 0.3, 0.35, and 0.4 cycles/degree (c/d). Animals were acclimated to the apparatus for 10 min per animal at least one day prior to collecting testing data. Animals that were unable to balance themselves on the platform were excluded from testing. Video data was analyzed blinded to mouse identity and condition. Clockwise and counterclockwise responses were measured and compared as a group, such that each animal contributes two datapoints (one result per direction), since each eye is differentially affected in the disease course and contributes to the clockwise vs. counterclockwise response.

Tissue collection

Mice were perfused sequentially with ice-cold PBS and 4% paraformaldehyde (PFA). Eyes and optic nerves were dissected out and post-fixed in 4% PFA for 24 h. For cryopreserving for cross sectioning, tissue was rinsed with PBS and put in 30% sucrose for 24 to 72 h, mounted in optimal cutting temperature reagent (OCT), flash-frozen with liquid nitrogen, and stored at -80 until cryo-sectioning. Retina and optic nerve sections were cut to a thickness of 12 μ m. For wholemount retinas, retinas were dissected out of the eye globe kept in PBS at 4°C until further processing.

Retinal flat-mount immunohistochemistry

Retinae were washed three times with wash buffer (0.5% Triton X-100 in phosphate buffer solution (PBS)), then blocked and permeabilized overnight at 4°C in blocking buffer (5% normal donkey serum (NDS), 2% Triton X-100 in PBS). Retinae were incubated in staining buffer (2% NDS, 0.5% Triton X-100 in PBS) with primary antibodies for 72 h at 4°C. Afterward, retinae were washed 3 times for 10 min with wash buffer and incubated in secondary antibodies overnight in staining buffer. Retinae were washed again 3 times for 10 min with wash buffer, 1 time for 10 min with PBS, then mounted on slides with coverslips and Fluoromount G and left overnight at room temperature to cure.

Retinal cross-section immunohistochemistry

Slides were thawed at room temperature for 5 min. For citrate antigen retrieval, slides were rehydrated first with ddH₂O, then saturated with citrate buffer and heated to 90°C for 10 min. Afterward, slides were rinsed with room temperature citrate buffer. Slides were then washed three times for 5 min with 1X PBS, blocked and permeabilized in blocking buffer (5% DS, 0.2% Triton X-100 in PBS), and incubated overnight at 4°C in staining buffer (1% DS, 0.2% Triton X-100 in PBS) and primary antibodies. The next day, slides were washed three times for 5 min with 0.2% Triton X-100 in PBS, then incubated for 2 h at room temperature in staining buffer with secondary antibodies and Hoechst (1:1000). Slides were washed again three times 5 min with PBS, before mounting a coverslip, and curing overnight.

Optic nerve cross-section immunohistochemistry

Slides were thawed at room temperature for 5 min, then washed three times with PBS following blocking and permeabilization in blocking buffer. Optic nerves were then incubated overnight in staining buffer and primary antibodies. The next day, slides were washed three times for 5 min with 0.2% Triton X-100 in PBS, then incubated for 2 h at room temperature in staining buffer with secondary antibodies and Hoechst. Slides were washed again three times 5 min with PBS, before mounting a coverslip, and curing overnight.

Hematoxylin and eosin staining

Retinal cross sections were stained with hematoxylin and eosin (H&E) using the Abcam H&E Staining Kit. Slides were first rehydrated with PBS for 3 min, then with ddH₂O for 3 min before being submerged in Hematoxylin Solution for 30 s. After two 30-s washes with ddH₂O, Bluing Reagent was applied to slides for 15 s. Slides were washed again with ddH₂O and submerged in ascending concentrations of ethanol before being saturated with Eosin Y solution for 20 s. Tissue sections were then dehydrated in two changes of 95% ethanol, followed by three changes of 100% ethanol. Sections were cleared in three changes of xylene and coverslipped using Permount Mounting Medium. Imaging was performed using the Zeiss AxioImager M1 microscope at 20x magnification.

Imaging and analysis

Images were acquired using Zeiss LSM 880 and 900 confocal microscopes with Zen software at the Montreal Neurological Institute microscopy core facility. Imaging parameters were kept the same between samples on the same slides and within the same groups. Automated analysis of nuclear fluorescence intensity was conducted for H3K27me3 in the RGC layer of cross-sections using a custom ImageJ macro. Counts of γ H2AX + RGCs and altered lamina RGCs were conducted manually, blinded to treatment condition. RBPMS+ RGC cell counts were conducted automatically using a custom ImageJ macro from 6 evenly spaced regions of interest from each retina. Retinal layer thickness was conducted manually in ImageJ, taking 3 width measurements of the IPL, INL, and entire

retina per image for at least two separate images from different retina locations for each biological replicate. Optic nerve blebs were quantified using automated thresholding and particle counts in ImageJ. For visualization of γ H2AX foci in RGCs, imaging was performed using a confocal laser scanning microscope (Zeiss LSM880) equipped with an Airyscan detector. Airyscan images were acquired in SR (super-resolution) mode using a 63x oil immersion lens with a numerical aperture of 1.4. Z-stacks were collected using a slice interval of 0.5 μ m and 25–30 slices per field of view, with a zoom of 1.8 and frame size of 1532 \times 1532 pixels. Raw Airyscan images were processed using the Airyscan Processing function of the Zen Black software in 3D mode, with a Wiener filter strength of 6. Imaging parameters were kept the same between samples.

Fluorescence-activated cell sorting of RGCs

Mice were euthanized with CO₂, then eyes were carefully removed with forceps. The retinae were immediately dissected out in cold Leibovitz-15 media and transferred to falcon tubes containing papain (10U/mL) and DNase in EBSS. Papain digestion was performed at 37°C for 10 min, after which retinas were gently triturated to a single cell suspension. Ovomucoid solution was layered underneath the papain-single-cell suspension, and cells were spun down for 7 min at 1000 rpm. The papain/ovomucoid mixture was removed carefully as to not disturb the cell pellet, and then the pellet was resuspended in cold HBSS with 1% N2/B27 supplements and filtered through a 40- μ m mesh filter. Cells were stained with anti-CD90.2 and live-dead dye for 30 min, then spun down and resuspended in HBSS with 1% N2/B27 supplements. All data was acquired on the FACS Aria Fusion (Becton-Dickinson Biosciences). Voltages were set up according to optimal PMT sensitive using the peak 2 (Spherotech) voltration technique. The nozzle used was 100 μ m at 20 psi. Doublet discrimination and dead cells were removed from sorting. Using the appropriate FMO control samples, a gate was drawn to select YFP/Thy1 double-positive cells. Double-positive cells were sorted into HBSS with 1% N2/B27 and held at 4°C until sort completion and downstream processing (Figure S1).

ATAC-sequencing

Approximately 15–50 thousand cells were pelleted after FACS isolation by centrifuging at 500g for 5 min at 4°C. The pellet was carefully resuspended in 50 μ L of cold lysis buffer (10 mM Tris-HCl, pH 7.4, 10 mM NaCl, 3 mM MgCl₂, 0.1% IGEPAL CA-630), then immediately centrifuged at 4°C, 500g, for 10 min. The supernatant was pipetted off, and the pellet was resuspended in 50 μ L of transposition buffer (25 μ L Tagment DNA Buffer, 2.5 μ L Tagment DNA enzyme 1, 22.5 μ L nuclease free H₂O) and incubated at 37°C for 30 min. After transposition, DNA was isolated using the Zymo ChIP DNA Clean & Concentrator Kit per manufacturers instructions, and eluted in 11 μ L of 10 mM Tris Buffer, pH 8.0. Library preparation was done using Nextera primer sequences and NEB Next High Fidelity 2X PCR master mix (M0541L) and amplification was run for 10 cycles. 40 base-pair paired-end sequencing was performed on a NextSeq500, and sequences were demultiplexed with 0 mismatches using bcl2fast1 2.20. Reads were trimmed with trimomatic, aligned to the genome with bowtie2, and quantified within 1000 bp of annotated transcription start sites in VisR.⁸⁸

RNA sequencing

Approximately 15–50 thousand cells were used per sample. Total RNA extraction was performed using the Qiagen miRNeasy kit according to manufacturer recommendations. 75 bp single-end sequencing was performed on a NextSeq500, and sequences were demultiplexed with 0 mismatches using bcl2fast1 2.20. Reads were trimmed with cutadapt, aligned with hisat2, and count matrices were generated by htseq. DESeq2 was used for count normalization and differential gene expression analysis. Pathway analysis was conducted with GSVA package for single-sample GSEA on the normalized counts table, and ClusterProfiler using the fgsea algorithm for ranked list GSEA.^{80,82} Pathway overrepresentation analysis was conducted using the enrichGO function in ClusterProfiler.

Gene coexpression analysis

Gene co-expression analysis was conducted using SimpleTidyGeneCoEx workflow, which uses Leiden based clustering to group genes based on their common changes in expression across the sample sets.⁸¹

Single-cell sequencing data analysis

The single-nucleus RNA sequencing (snRNA-seq) data in this study were obtained from a previously published dataset by Schirmer et al. in 2019, accessible under accession number PRJNA544731 (NCBI Bioproject ID: 544731).⁴⁶ This dataset comprises gray matter tissue samples from eleven patients diagnosed with multiple sclerosis (MS) and nine control samples. The MS patient samples include those derived from acute-chronic active lesions and chronic inactive lesions of progressive forms of MS. To dissect the snRNA-seq data, we employed a well-established workflow with the Seurat package, encompassing processes such as dimensionality reduction, cell type identification, gene expression normalization, and clustering.⁹³ Specifically, cells with a mitochondrial gene composition of 5 percent or higher were classified as non-viable and were consequently excluded from further analysis. Likewise, cells with fewer than 200 or more than 2500 unique feature counts were deemed low-quality cells and were also removed from downstream analysis. Following quality control procedures, the gene expression profiles of the remaining cells were subjected to natural log normalization and scaling. Principal component analysis (PCA) was performed on highly variable genes to reduce the dimensionality of the dataset. Subsequently, the first 20 principal components were selected for clustering analysis. We constructed a shared-nearest neighbor graph based on the results of the PCA, and the Louvain clustering algorithm was employed iteratively to identify clusters at multiple resolutions. For this analysis, we used a resolution parameter of 0.6. Finally, we harnessed the uniform manifold

approximation and projection (UMAP) algorithm to visualize the identified clusters in a two-dimensional space. Cell types were annotated using reference publication of Schirmer et al., datasets and clusters renamed based on their cell identities. To facilitate later analyses, we limited our analysis to neuronal cells with greater than 5 cells per cluster per condition (Control vs. MS) in this dataset then we extracted and compiled the average expression levels of these neurons, stratified by patient.

Human brain tissue immunohistochemistry

Autopsy samples were preserved within 4h postmortem, and lesions classified using Luxol Fast Blue/Haematoxylin & Eosin staining as previously published and to identify cortical tissue regions in samples.^{94–96} Sections were on-slide fixed in acetone for 10 min, blocked in 10% serum for 1 h at RT, and immunolabeled with primary antibodies against NEUN and γ H2AX overnight at 4°C in 5% serum, with 0.5% Triton X-. This was followed by secondary antibody incubation for 1 h at room temperature, DAPI staining, and incubation with Sudan Black (0.3% in 70% alcohol) to reduce tissue autofluorescence. Slides were then cover-slipped slipping and dried overnight. Images were acquired on an LSM900 microscope, retaining the same laser settings between slides. 2 ROIs per control patient sample ($n = 2$) and 4 ROIs per MS patient sample ($n = 3$) were collected and analyzed in ImageJ. NEUN+ thresholds were made and the max and mean pixel intensity within each NEUN+ cell was measured in the γ H2AX channel. Measurements were down sampled to 50 datapoints per sample ($n = 100$ total for control, $n = 150$ total for MS patient tissue).

QUANTIFICATION AND STATISTICAL ANALYSIS

Statistical analysis was conducted in R for analyses relating to gene expression and sequencing analysis, and GraphPad Prism 8.0 for all other analyses. Information on the statistical tests performed and software used, number of replicates, and error measures can be found in the figure legends for each experiment. Significance was defined as p value < 0.05 , with some experiments assessing only comparisons where the adjusted p values < 0.1 . All animals were randomly assigned to treatment and control groups.